Development of Emissive Porous Polymers and Parabolic Trough Underside Reflectors for Enhanced Radiative Cooling

Po-Chun Chiu

A THESIS SUBMITTED TO
THE FACULTY OF GRADUATE STUDIES
IN PARTIAL FULFILLMENT OF THE REQUIREMENTS
FOR THE DEGREE OF
MASTER OF SCIENCE

GRADUATE PROGRAM IN MECHANICAL ENGINEERING
YORK UNIVERSITY
TORONTO, ONTARIO

December 2025

Abstract

A trough-enhanced radiative cooling (RC) system was developed and experimentally evaluated to achieve high-efficiency passive cooling under real outdoor conditions. Polymer-based porous PVDF-HFP emitters with high solar reflectance and strong atmospheric emittance were fabricated and integrated with parabolic trough reflectors. Monte Carlo ray tracing and heat balance simulations were conducted to predict temperature performance under various solar irradiance and convection scenarios. The experimental results revealed stable sub-ambient cooling of 1.2–4.2 °C during the day and up to 4 °C at night, demonstrating consistent cooling even under partial cloud coverage. Numerical predictions agreed well with measurements, showing less than 1 °C deviation, indicating the model's reliability in evaluating RC performance. The validated model enables predictive design and optimization of trough-integrated RC systems, while the findings highlight the potential of reflective geometries in enhancing cooling power and scalability for energy-efficient thermal management and sustainable building applications.

Acknowledgments

As I reach the conclusion of my Master of Engineering journey, my reflection is not only on the academic and scientific achievements I have gained, but also on the invaluable personal growth I have experienced throughout this process.

First and foremost, I would like to express my heartfelt gratitude to **The Buddha** and **Master Zhen-Ru** for guiding me with wisdom and peace along this journey. Through this experience, I have come to know myself more deeply, discovering inner strength I had yet to realize — including a sense of inclusiveness toward all beings, responsibility for the world, and the spirit of critical thinking.

I would like to extend my deepest appreciation to my supervisors, **Professor Paul G. O'Brien** and **Professor Siu-Ning Leung**, for their continuous support, invaluable guidance, and insightful feedback throughout my research and studies. Their expertise, patience, and encouragement have been essential in shaping this work and in broadening my academic perspective.

I am also sincerely grateful to my committee member, **Professor Thomas Cooper**, for providing constructive comments and valuable discussions that helped refine the quality of my thesis.

Finally, I would like to express my deepest gratitude to **my family** for their unconditional love, understanding, and unwavering support throughout my studies in Canada. Their constant encouragement gave me the courage to overcome challenges and the motivation to pursue my goals with determination. Without their belief in me, this accomplishment would not have been possible.

Thank you to everyone who played a role in this journey; your support and encouragement have been invaluable in helping me become who I am today.

Table of Contents

List of Tables

Table of Figures

Chapter 4

List of Abbreviations and Acronyms

DI	Deionized
EEI	Earth's Energy Imbalance
FIR	Far-Infrared
FTIR	Fourier Transform Infrared
GUM	Guide to the Expression of Uncertainty in Measurement
h-BN	Hexagonal Boron Nitride
LWIR	Long-Wave Infrared
MIR	Mid-Infrared
MCRT	Monte Carlo Ray Tracing Method
MTPS	Modified Transient Plane Source Method
NIR	Near-Infrared
PDRC	Passive Daytime Radiative Cooling
PVDF-HFP	Poly(vinylidene fluoride-co-hexafluoropropylene)
RC	Radiative Cooling
UV	Ultraviolet
VIS	Visible
WVIPS	Water Vapor-Induced Phase Separation

List of Symbols

A_{RC} Emitting surface area of the RC emitter

A_{atm} Emitting surface area of the atmosphere

C_g Geometric solar concentration ratio

C_P Specific heat capacity of the fluid

c Speed of light

D_{RC} Diameter of the tubular radiative cooler

D_{pipe} Outer diameter of the copper pipe

f Focal length

$F_{abs,\ \delta\text{-}\gamma}$ Fraction of rays that propagate into outer space in a direction with a zenith angle between δ and γ radians

$F_{RC\text{-}space}$ The view factor from the RC surface to space

$F_{RC\text{-}atm}$ The view factor from the RC surface to atmosphere

$F_{RC\text{-}earth}$ The view factor from the RC surface to earth

H Trough height

h Convective heat transfer coefficient

h_p Planck's constant

I_{atm} Spectral intensity of the atmosphere

k Thermal conductivity

K_b Boltzmann constant

k_C Coverage factor

L_{RC} Length of the tubular radiative cooler

Mn Weight-averaged molecular weight

Mw Number-averaged molecular weight

m Fluid mass

P_{atm} Incoming absorbed atmospheric radiation

$P_{cooling}$ Net cooling power

P_{earth} Incoming radiation from the earth absorbed by the RC

P_{nonrad} Nonradiative heat transfer

$P_{diffuse}$ Diffuse solar radiation

P_{direct} Direct solar radiation

P_{RC}	Outgoing radiative power from the RC
$P_{RC\text{-}earth}$	Outgoing radiative power from the RC to earth
$P_{RC\text{-}space}$	Outgoing radiative power from the RC to space
P_{solar}	Incoming absorbed solar radiation
P_{space}	Incoming absorbed radiation from space
$\mathbf{R}$	Ray's propagating directional vector
R_t	Total thermal resistance of the tubular configuration
R_{fluid}	Thermal resistance of the internal fluid
R_{pipe}	Thermal resistance of the copper pipe
R_{RC}	Thermal resistance of the RC membrane
R_{tape}	Thermal resistance of the thermal tape
T	Temperature
T_{atm}	Atmospheric temperature
T_{air}	Ambient air temperature
T_{earth}	Earth's temperature
T_{fluid}	Mean fluid temperature
$T_{pipe,\ in}$	Interface temperature between fluid and copper pipe
T_{RC}	Radiative cooler temperature
$T_{RC,\ in}$	Interface temperature between the thermal tape and the RC membrane
$T_{RC,\ out}$	Outer surface temperature of the RC membrane
$T_{RC\text{-}ss}$	Steady-state temperature of the radiative cooler
T_{space}	Temperature of outer space
T_{tape}	Interface temperature between the thermal tape and copper pipe outer surface
t_{foil}	Thickness of the non-reflective black aluminum foil tape
t_{pipe}	Wall thickness of the copper pipe
t_{RC}	Thickness of RC membrane
t_{tape}	Thickness of the thermal adhesive tape
W_{trough}	Top opening width of the parabolic trough
x, y, z	Cartesian coordinate system axis
$\mathbf{Z}$	z-axis vector
$\oiint dA$	Surface integration over the RC emitter
α	Total absorptance

α_λ'	Spectral directional absorptance
α_{solar}	Solar energy absorption
ε	Emittance
ε_{atm}	Emittance of the atmosphere
ε_{earth}	Emittance of the earth
ε_{RC}	Emittance of the RC
ε_{space}	Emittance of outer space
ε_λ'	Spectral directional emittance
θ	Zenith angle
θ_{int}	The zenith angle of a ray intercepted by a fictitious surface
θ_s	The acceptance angle of the trough
ϕ	Planar azimuthal angle
ρ	Reflectance
ρ_λ'	Spectral directional reflectance
τ	Total hemispherical transmittance
$\tau_{atm,0}$	Spectral atmospheric transmittance in the normal direction
τ_λ'	Spectral directional transmittance
λ	Wavelength
δ	Angle increment lower limit
γ	Angle increment upper limit
∞	Infinity

Chapter 1–Introduction

1.1. Background and Context of the Research

The main objective of the United Nations Environment Programme is to take immediate action to address the urgent concerns related to climate change by reducing greenhouse gas emissions. According to the report entitled, “Tracking Changes in Earth's Energy Budget” published by NASA (2022) [1], the top-of-atmosphere (TOA) imbalance, also known as Earth's energy imbalance (EEI), was estimated to be 0.71 W/m^2. This positive value indicates more radiant energy from the sun is entering the atmosphere as compared to the radiance emitted from Earth to outer space. The presence of greenhouse gases, including carbon dioxide (CO_2), methane (CH_4) and H_2O vapour, exacerbates the Earth's radiative energy imbalance by absorbing outgoing longwave radiation before it escapes into space, thereby intensifying the process of global warming. This leads to rising sea-levels, flooding and infrastructure damage.

One of the main factors that intensifies global warming is increasing energy demands for space cooling. Traditional cooling systems are energy-intensive, pollution-emitting, and exhibit low efficiencies. According to the International Energy Agency's expectations, due to climate change and population growth, the demand for air conditioning units is projected to nearly triple, from 1.5 billion to 4.4 billion, by 2050 [2]. In other words, approximately 5200 TWh of electricity for

space cooling. These facts are alarming and highlight the urgency to explore new cooling strategies that are sustainable, cost-effective, have low environmental impact and reduce energy consumption.

One of the most common technologies to reduce global warming is carbon capture, as increased global warming potential since the industrial era is primarily attributed to anthropogenic CO_2 emissions. With decades of development and modification, radiative cooling (RC) materials have become cost-effective, scalable, and environmentally friendly applications for sub-ambient cooling. RC materials exhibit a high emittance over the wavelength range from 8-13 μm, which is referred to as the IR atmospheric window. Radiation directed toward outer space is negligibly absorbed over the atmospheric window. The existing large temperature difference between the average sea-level temperature (~288 K) and outer space (~2.7 K), causes a net radiative heat flux that can dissipate a significant amount of radiation into space. Since the temperature of space is about 2 K, the radiant power transferred from space to Earth over the atmospheric window is negligible. This radiative cooling mechanism provides a new method to deal with the trapped heat in the atmosphere rather than capturing CO_2 emitted to the atmosphere.

1.2. Statement of the Problem

Designing RC materials with high emittance over the atmospheric window to achieve a strong radiative exchange with outer space provides an effective means of passive cooling [2]; however, several important questions remain: (i) the absorption of unwanted heat from the surroundings, including solar radiation, atmospheric radiation, earth radiation and non-radiative heat, significantly reduces the performance of RC materials. (ii) how to economically integrate RC materials into effective cooling system.

Passive daytime RC (PDRC) materials must also possess a high reflectance over the solar spectrum to prevent the heating that occurs when sunlight is absorbed [3], [4]. As reported in the literature, the PDRC must exhibit a solar reflectance of 0.9 or greater to achieve effective cooling performance.

Radiation is emitted from the atmosphere over a broad spectral range, and the amount of this radiation that is incident onto the PDRC material is strongly affected by the climate condition. Furthermore, the amount of radiation from the earth and surrounding terrestrial surfaces that is incident onto the PDRC is dependent on the location where it is installed and the nearby infrastructure. Non-radiative heat exchange, such as conduction and convection, between the PDRC and its surroundings typically reduce the sub-ambient cooling effect induced by PDRC materials. The methods used to decrease unwanted heat gain require further investigation, design and development to achieve widespread implementation of PDRC materials.

Another critical consideration is the capability of integrating PDRC systems into existing cooling infrastructures. The PDRC serves as a heat exchanger between earth and outer space. Radiant heat can easily pass through the atmospheric window into space. However, the intrinsic thermal conductivity of PDRC materials plays a dominant role in how efficiently heat from a fluid can be rejected into the cold reservoir (outer space). If the PDRC has a high thermal resistance, it is unable to transfer heat effectively, even though it can achieve a sub-ambient cooling.

Moreover, PDRC structures are commonly mono-facial and effective cooling can only occur on sky-facing surfaces, In contrast, surfaces directed towards earth or other infrastructure contribute little or no cooling effect. In the literature, bifacialized PDRC are used to induce radiative heat exchange between non-sky-facing surfaces of PDRC structures and outer space by parabolic

reflectors. This shows promising advantages compared to conventional PDRC structures. There are still several unexplored questions to answer in order to gain insight about how reflectors benefit PDRC structures. First, the influence of RC and reflector geometry on the redirection of radiation and its zenith angle distribution requires further investigation. Second, the impact of concentrated solar radiation induced by the parabolic trough on the net cooling power has not been sufficiently addressed. Closing these research gaps is required to promote the cooling efficiency, which is hindered by unwanted heat gain, limited effective radiating surface area and RC thermal conductivity.

1.3. Objectives of the Research

The overarching goal of this research is to develop and evaluate novel configurations of micro and nano-structured PDRC materials integrated with parabolic trough reflectors, thereby enhancing their cooling performance under daytime operating conditions. To achieve this goal, the following specific objectives are pursued:

1 Numerical modelling of RC performance within parabolic trough systems

A comprehensive numerical framework is developed to evaluate the cooling performance of RC emitters located along the focal line of parabolic trough reflectors. Monte Carlo Ray Tracing (MCRT) methods are employed to examine:

1.1 The influence of RC geometrical parameters (e.g., diameter, length), and trough geometrical parameters (e.g., height, length, focal length) on cooling power and equilibrium temperature.

1.2 The impact of environmental conditions, including absorbed solar radiation, convective

heat transfer from ambient air, and atmospheric radiative exchange.

1.3 Forward MCRT is applied to quantify emission from RC surfaces, while reverse MCRT is adopted to calculate absorbed radiation. The methodology also critically evaluates the validity of assumptions in existing literature, highlighting limitations and justifying the modelling framework.

This objective provides the first systematic analysis of RC emitters coupled with parabolic troughs, with results normalized by focal length for general applicability.

2 Fabrication and optimization of RC materials

Fabricate RC emitters comprised of PVDF-HFP-based films and systematically characterize their optical and thermal properties. The study emphasizes:

2.1 The identification of optimized emitter samples through evaluation of spectral solar reflectance, atmospheric window emittance, thermal conductivity, and film thickness.

2.2 Optimization of the optical property through film thickness variation.

2.3 Fabricate enough samples to cover a copper pipe with length of 0.5 m and diameter of 1 inch.

This objective provides the material foundation for practical implementation of trough-enhanced RC systems.

3 Experimental validation of trough-enhanced RC systems

Construct and test a parabolic trough-integrated RC system under outdoor conditions to demonstrate a proof of concept and to verify numerical predictions. The study compares the performance of a tubular RC emitter with that of a blackbody emitter positioned along the trough focal line, which also incorporates an underside flat blackbody surface for reference.

Performance is evaluated over a 24-hour testing period, considering uncertainties from solar radiation measurements and convection heat transfer estimation. The results not only demonstrate proof of concept but also serve as experimental validation for the modelling and material development stages.

Together, these objectives integrate theoretical and experimental approaches to advance the design and evaluation of trough-assisted RC systems.

1.4. Thesis Outline

This thesis presents a comprehensive investigation of parabolic trough-assisted PRDC systems, focusing on performance enhancement mechanisms, material innovations, and experimental validation. The thesis is organized as follows:

Chapter 2 reviews the current state of RC technology, including material design, tailoring optical and thermal properties, integrating strategies, and limitations. The chapter situates trough-assisted RC within the broader context of passive and energy-efficient cooling solutions.

Chapter 3 presents the Monte Carlo Ray Tracing (MCRT) framework developed to simulate the cooling performance of RC emitters integrated with parabolic troughs. The analysis demonstrates the role of dual-surface emission and reflector redirection in improving cooling performance.

Chapter 4 presents the fabrication of polymer-based RC emitters, including detailed characterization of their optical, thermal, and structural properties. Optimized samples are identified, and reproducibility between laboratory-scale and scaled fabrication is assessed to establish the material foundation for system-level validation.

Subsequently, the construction of the trough-integrated RC system is described, followed by results from a 24-hour outdoor testing campaign. Tubular RC emitters and blackbody emitters are directly compared within trough reflectors, while a flat blackbody surface configuration is employed as a reference. The experimental findings confirm the numerical model's predictive capability and highlight the performance enhancement achieved by the parabolic trough configuration.

Chapter 5 summarizes the contributions of the thesis, identifies limitations and outlines potential direction for future research, including advanced material integration, durability assessment, and system-level optimization.

Chapter 2–Literature Review

2.1. Introduction

Radiative cooling (RC) materials offer a passive, energy-free cooling strategy by emitting infrared radiation through the 8-13 μm atmospheric transparency window, where thermal radiation can escape directly to outer space. Since the temperature of space is about 2.7 K, RC materials with high emittance in this spectral window can achieve effective passive sub-ambient cooling while receiving negligible amounts of radiant power transferred from space [2]. To achieve effective passive cooling under direct sunlight, daytime RC materials must also exhibit high reflectance to avoid radiative heating that occurs when sunlight is absorbed [3], [5].

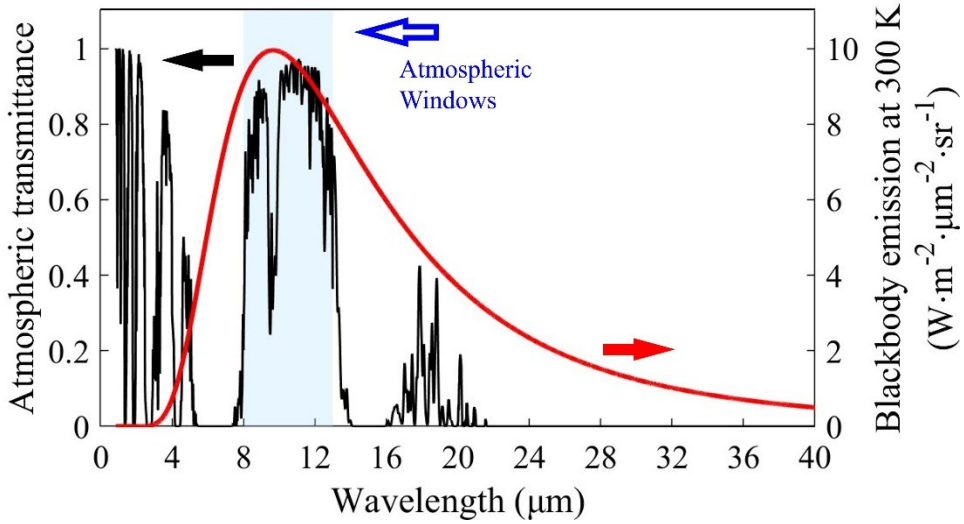

Figure 2-1. Atmospheric spectral transmittance obtained from ATRAN and the blackbody spectral emission at 300 K.

2.2. Fundamentals of Radiative Cooling

RC is governed by the fundamental mechanisms of heat transfer between a sky-facing surface, the atmosphere, outer space, and surrounding terrestrial elements. An RC surface emits thermal radiation (P_{RC}), which serves as the primary driver of cooling. In principle, outer space can be considered an ideal heat sink due to its extremely low effective temperature. The radiative exchange with space (P_{space}) is therefore negligible compared with other heat flux components.

A unique feature of RC lies in the atmospheric transparency window (approximately 8–13 μm in the mid-infrared region). Within this spectral range, thermal radiation emitted from the RC surface can pass through the atmosphere with minimal absorption and directly escape into outer space, thereby enabling passive cooling below ambient temperature. Radiation emitted outside this window, however, is largely absorbed by atmospheric constituents such as water vapor and carbon dioxide. The absorbed energy is partly re-emitted into space and partly redirected back toward the Earth, contributing to the terrestrial energy balance.

During daytime operation, an RC surface is also subjected to additional heat fluxes. These include the absorption of incident solar radiation and, depending on the system orientation and surrounding environment, the absorption of terrestrial longwave radiation (P_{earth}) emitted by adjacent surfaces. Both of these inputs counteract the cooling effect and thus need to be mitigated through material design and system configuration.

In addition to radiative exchange, non-radiative heat transfer processes, including convection and conduction, play a critical role in determining the overall cooling performance. These mechanisms typically act in opposition to sub-ambient cooling by facilitating heat gain from the warmer

surrounding air or supporting structures. Minimizing non-radiative contributions is therefore essential to achieving efficient passive daytime radiative cooling.

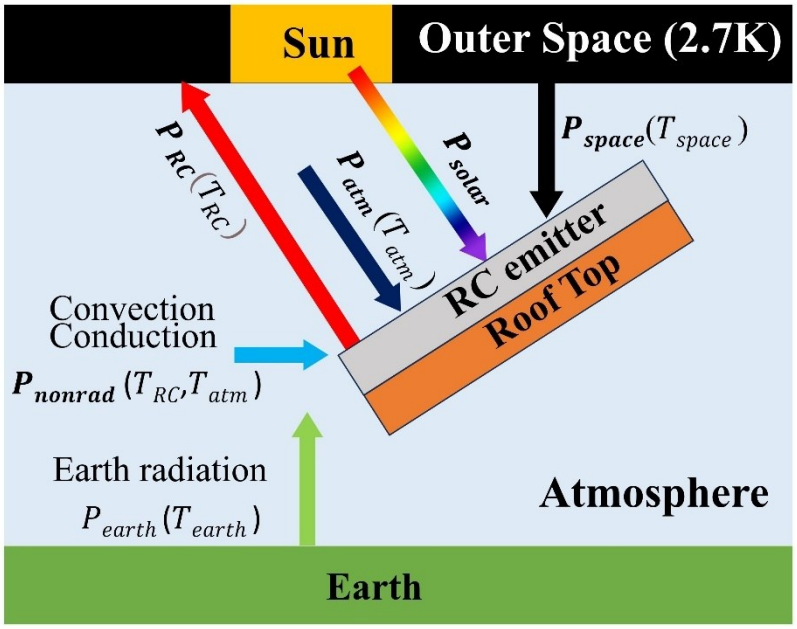

Figure 2-2 : Heat transfer mechanisms for a RC panel

2.3. Radiative Cooling Materials and Innovative Applications

Over the past decades, a wide range of RC materials have been developed to be used for cost-effective, scalable, and environmentally friendly technology to achieve sub-ambient radiative cooling [5]. These include polymers [4], [7], [8], inorganic solids [8], [9], [10], [11], and inorganic-polymer hybrids [12], [13]. These materials have been fabricated into different configurations such as photonic structures [14], [15], [16], multilayer membranes [12], [18], [19], [20], [21], porous coatings [16], [21], [22], and pigmented white paints [9], [10]. For instance, Cheng et al. [22] proposed a hierarchically micro- and nano-porous-structured PVDF-HFP membrane manufactured

using water vapor-induced phase separation (WVIPS) with electrospinning, achieving 93.7% solar reflectance and 91.9% emittance within the atmospheric window. Furthermore, Pirvaram et al. [24] fabricated a porous poly(vinylidene fluoride-co-hexafluoropropylene) [P(VdF-HFP)] membrane using the phase inversion method. The membrane possesses solar reflectance and emittance over the atmospheric window as high as 0.982 and 0.985, respectively. Pirvaram et al. [24] predicted that covering just 1% of earth's surface with such RC materials could reverse the Earth's Energy Imbalance (EEI), which would cause a global cooling effect. In addition, Ma et al. [25] reported the development of a multilayer emitter, consisting of seven layers of SiO_2 and Si_3N_4 films, that achieved a high solar reflectance of 0.97 and an average emittance of 0.75 within the atmospheric window.

RC configurations reported in the literature have achieved high cooling performance in practical outdoor conditions. Zhai et al. [8] developed a metamaterial-based RC composed of randomly embedded resonant polar dielectric microspheres within a polymeric matrix, achieving an emittance of 0.93 and a solar reflectance of 0.96. Under a solar irradiance of 900 W/m^2 in Arizona, USA, the RC exhibited a noontime radiative cooling power of 93 W/m^2. Moreover, an average cooling power of 110 W/m^2 was sustained over a continuous 72-hour measurement period. Mandal et al. [26] fabricated a hierarchically porous polymer coating composed of P(VdF-HFP) which achieved an atmospheric window emittance of 0.97 and a solar reflectance of 0.96. The coating enabled a sub-ambient temperature reduction of 6 °C and delivered an impressive cooling power of 96 W/m^2 under a solar irradiance of 890 W/m^2 and ambient temperature of 26 °C in Phoenix, USA. The coating also demonstrated excellent durability, with only minimal changes observed after a month-long outdoor exposure in New York City.

Innovative diurnal RC structures can be integrated into energy-saving systems through various approaches, including integration with building cooling systems [11], [27], [28], photovoltaic panels [29], [30], [31], solar collectors [32], [33], [34], or by serving as a coating or shielding for rooftops [35], [36], [37]. Fang et al. [35] demonstrated the potential of energy-saving achieved by using a cool roof metamaterial film (RadiCold) that exhibits an exceptionally high solar reflectance of 0.96 and emittance of 0.93 within the atmospheric window. Their study showed that integrating a RadiCold rooftop with an air-conditioning system (COP = 3.0) resulted in electricity savings ranging from 113.0 to 143.9 kWh m^{-2} yr^{-1}.

Chapter 3–Numerical Analysis of the Effects of Underlying Trough Reflectors on the Performance of Tubular RCs

3.1. Introduction

One limiting factor hindering the widespread adoption of RC structures is their mono-facial configuration. They are only cooled by their sky-facing surfaces, while the bottom surface contributes little or no cooling [38]. Several studies have investigated the integration of the RC downward-facing, non-participating surface into RC systems by employing an underside reflector to convert them into a bifacial configuration [39], [40], [41]. Peoples et al. [39] introduced a V-shaped trough reflector, which they stated doubles the net cooling power by utilizing the bottom surface of the RC as an active participant. In this case, the net cooling power was calculated by utilizing both the sky-facing and bottom-facing surfaces of the tubular RC to enhance cooling performance.

Another limitation of the RCs lies in the atmospheric radiation they receive, particularly from higher zenith angles. At a zero-zenith angle (in the direction straight upwards from the Earth's surface), the atmosphere has the highest transmittance and emits the least amount of radiation to

earth. As the zenith angle increases, the optical pathlength through the atmosphere extends, leading to a higher air mass (AM) and increased atmospheric thermal radiation incident onto the RC surface from oblique directions. [41], [42], [43].

An effective strategy to enhance the net cooling performance of RCs is to utilize underlying parabolic reflectors to block radiation incoming from the surroundings, including radiation from the ground, atmospheric radiation incident from large zenith angles, and solar radiation. The parabolic reflector redirects radiation from the RC towards the atmosphere at low zenith angles. For the ideal case in which the parabolic trough is a perfect reflector with an emittance of zero and when solar radiation is blocked, the only radiation the RC receives from the surroundings is atmospheric radiation incident from low zenith angles, which has a low intensity when the sky is clear.

The benefits of using parabolic trough reflectors [44], [45], [46], [47] and paraboloid dish reflectors [48] to enhance the performance of RC structures have been reported in the literature. Dan et al. [44] introduced compound parabolic concentrators combined with a flat mono-facial RC emitter, achieving an 18.1% enhancement in nighttime cooling compared to a RC with an inverted trapezoidal reflector. They demonstrated that the concentrator serves dual functions as a solar shade and wind shield during the daytime, effectively minimizing heat intrusion. Pirvaram et al. [48] investigated paraboloid dish reflectors positioned beneath the bifacial RC structure to enhance the effective radiative surface area and to maintain a small radiation zenith angle. Numerical results showed a paraboloid dish structure with a focal length of 100 mm and a height of 625 mm provides up to 200 W/m^2 of cooling power for a bifacial RC emitter and can achieve a sub-ambient temperature drop of 10 °C.

To date, the utilization of parabolic trough reflectors for enhancing bifacial-RC performance has yet to be investigated in a comprehensive manner. In particular, the effects of incident sunlight, convective cooling, and the geometry of the parabolic trough and RC structure, including reflector height, length and focal length have not yet been reported. In this work, the cooling performance of RCs located along the focal line of parabolic trough reflectors are modelled using both forward and reverse Monte Carlo ray tracing methods. The results from the numerical analysis provide the first comprehensive study on the cooling performance of bifacial-RC materials located along the focal line of parabolic trough reflectors. The cooling power of these RC materials is determined as a function of the reflector's geometry (i.e., the height and focal distance of the trough and the diameter of the object being cooled along the focal line). The cooling power of the RC structure is also determined as a function of the environmental conditions (i.e., heat gain due to solar radiation, convective heat transfer from the surroundings, and heat gain due to incident radiation from the atmosphere).

3.2. Methods

3.2.1. Description of the Radiative Cooling Structures and Underside Reflectors

Figure 3-1 presents six tubular RC configurations with emitter diameters ranging from infinitesimal (line-type) to finite values ($2f$). The six case studies were strategically selected to quantify the effect of a wide range of geometrical parameters on cooling performance. Each configuration has a fixed emitter length of 0.01 m and is distinguished by the geometries of their underlying reflectors. In Case 1, the tubular RC emitter is positioned horizontally above an infinite-area blackbody surface, with a finite separation to ensure optical decoupling (Figure 3-1a). In Case

2, the infinite-area blackbody is replaced with an infinite-area flat perfect reflector positioned beneath the RC emitter. (Figure 3-1b). In Case 3, the RC emitter is positioned 0.1 m above the center of a 1 m^2 flat perfect reflector which rests on top of an infinite blackbody surface (Figure 3-1c). The 0.1 m separation distance was selected based on the focal lengths of the parabolic troughs in Case 4 and Case 5, while the 1 m^2 reflector area corresponds to the projected area of the trough on the horizontal surface in Case 5. In Cases 4 to 6, three types of parabolic troughs are configured with tubular RC emitters centered along their focal lines. The surface of the trough can be described by the equation $z = y^2/(4f)$, where f is the focal length and the x, y and z axes are shown in Figure 3-1d. For Case 4 (Figure 3-1d), f = 0.1 m, the height of the trough is equal to the focal length, and the corresponding opening width is 0.4 m. For Case 5 (Figure 3-1e), f = 0.1 m, the width at the top of the trough is 1 m, and the corresponding height is 0.625 m. For Case 6 (Figure 3-1f), the trough is the same height as in Case 5 but with a narrower opening width of 0.4 m, which matches Case 4, and a corresponding focal length of 0.016 m. All troughs are 1 m long.

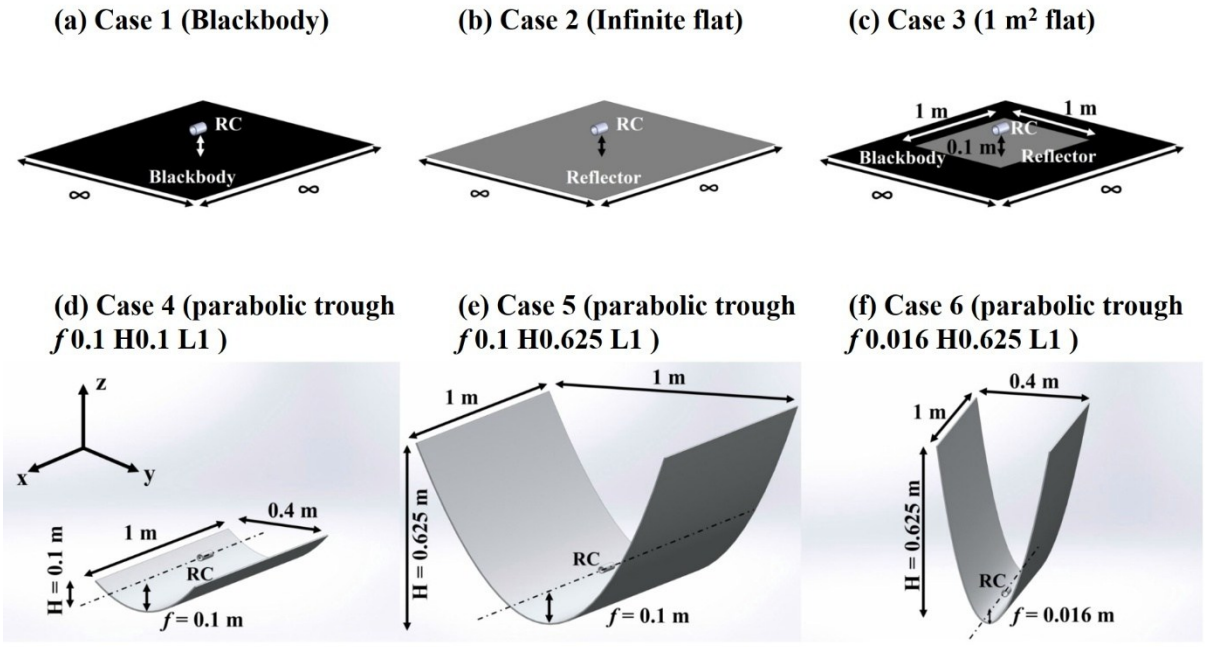

Figure 3-1: Schematic of the RC emitter within the six configurations investigated in this work

The reflective surfaces (i.e., the flat underlying surfaces for Cases 2 and 3 and the trough for Cases 4 to 6) are considered to be perfect specular reflectors with $\rho = 1$ for all wavelengths. For all cases, two different emittance spectra for the RC surfaces are considered when modelling the cooling power of the tubular RC structures.

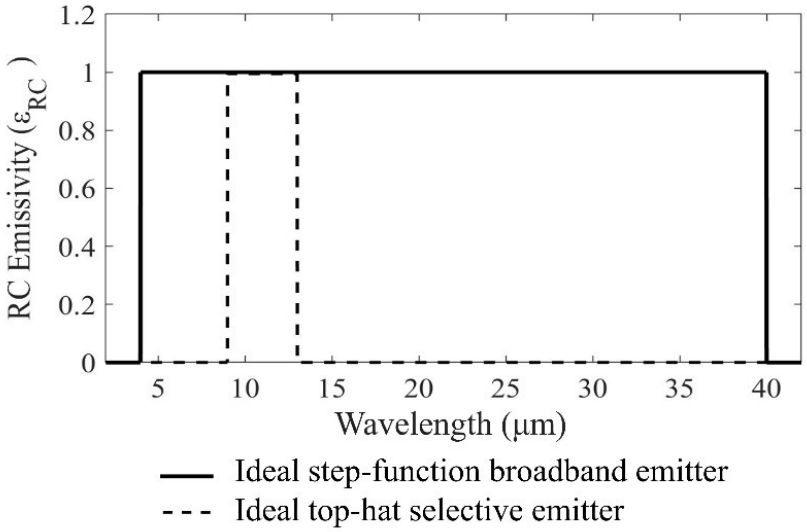

Figure 3-2: RC emittance spectra for an ideal step-function broadband emitter and an ideal top-hat selective emitter across different wavelengths.

As shown by the dashed line in Figure 3-2, the first emittance spectrum is an ideal "top-hat" function, with an emittance of 1 within the atmospheric window (8 to 13 μm) and 0 emittance for wavelengths outside this range. In the spectral regions where the emittance is 0 (outside the atmospheric window) the surface of the RC has a reflectance of 1, which is beneficial for reflecting incident radiation from the sun or atmosphere over these regions. The second emittance spectra, shown as the solid line in Figure 3-2 has the form of an ideal broadband emitter with an emittance of 1 between 4 and 40 μm. The emittance and reflectance outside this range is set to 0 and 1, respectively. The lower bound of the broadband emitter's wavelength range is set such that 99% of incident solar radiation is reflected. Additionally, approximately 5.5 % of the emissive power of a 300 K blackbody occurs at wavelengths above 40 μm.

3.2.2. *Cooling Performance Calculations*

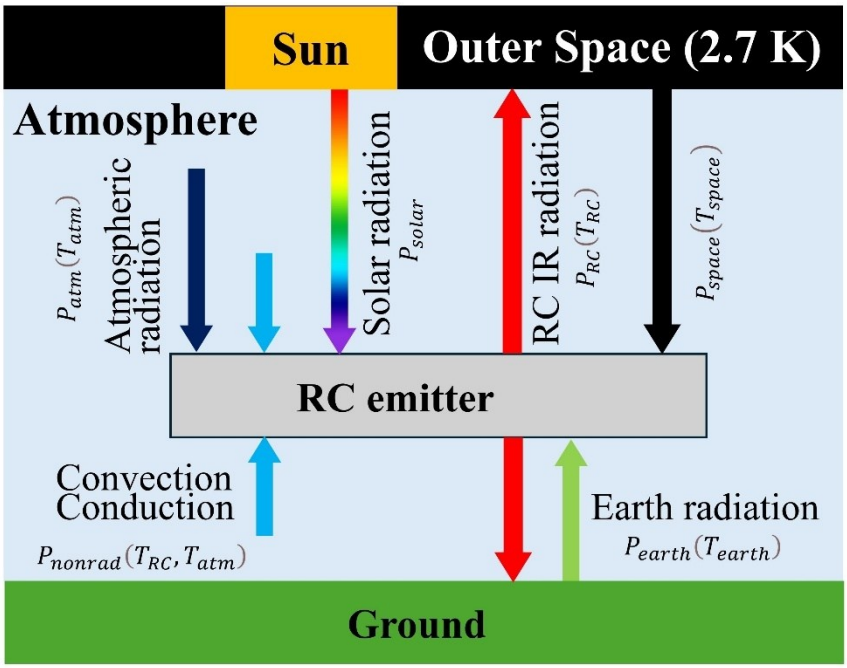

Figure 3-3**:** Heat transfer mechanisms for an RC emitter (P_{space} is negligible)

Figure 3-3 illustrates the six main heat transfer mechanisms that occur between the RC emitter and its surroundings. The total RC cooling power ($P_{cooling}$) can be obtained as a function of T_{RC}, T_{atm}, T_{earth}, T_{space} and P_{solar} as shown in Equation (3-1)

$$P_{cooling} = P_{RC}(T_{RC}) - P_{atm}(T_{atm}) - P_{earth}(T_{earth}) - P_{space}(T_{space}) - P_{solar} - P_{nonrad}(T_{RC}, T_{atm}) \quad (3\text{-}1)$$

P_{RC} represents the outgoing radiation from the RC surface toward the sky and earth. P_{atm} denotes the incoming radiation from the atmosphere absorbed by the RC surface, while P_{earth} refers to the incoming radiative heat transfer from the earth to the RC surface. P_{space} is the incoming radiation from outer space to the RC, which is negligible and assumed to be zero because of the low temperature of outer space. P_{solar} accounts for the incoming solar radiation. P_{nonrad} represents the heat transfer between the RC surface and the ambient atmosphere via convection and conduction,

and its sign can be either positive or negative. When heat is transferred from the ambient atmosphere to the RC surface, P_{nonrad} is positive. Conversely, P_{nonrad} is negative when heat is transferred from the RC surface to the ambient atmosphere. The numerical expressions used to determine each heat transfer term are provided in Equations (3-2) to (3-6).

$$P_{RC} = F_{RC-space} \int_0^{\emptyset} \int_0^{\theta} \sin\theta \cos\theta \int_0^{\infty} \varepsilon_{RC}(\lambda,\theta) I_{BB}(T_{RC},\lambda)\, d\lambda\, d\theta\, d\emptyset\, dA \tag{3-2}$$

$$P_{atm} = F_{RC-atm} \oiint dA_{RC} \int_0^{\emptyset} \int_0^{\theta} \sin\theta \cos\theta \int_0^{\infty} \varepsilon_{atm}(\lambda,\theta)\varepsilon_{RC}(\lambda,\theta) I_{BB}(T_{atm},\lambda) d\lambda d\theta d\emptyset \tag{3-3}$$

$$P_{earth} = F_{RC-earth} \oiint dA_{RC} \int_0^{\emptyset} \int_0^{\theta} \sin\theta \cos\theta \int_0^{\infty} \varepsilon_{earth}(\lambda,\theta)\varepsilon_{RC}(\lambda,\theta) I_{BB}(T_{earth},\lambda) d\lambda d\theta d\emptyset \tag{3-4}$$

$$P_{rad,\,solar} = \oiint dA_{RC}\,(C_g \cdot P_{direct} + P_{diffuse}) \tag{3-5}$$

$$P_{nonrad} = \oiint h \cdot \{T_{atm}(x,y) - T_{RC}(x,y)\} dA_{RC} \tag{3-6}$$

where $F_{RC\text{-}space}$, $F_{RC\text{-}atm}$ and $F_{RC\text{-}earth}$ are the view factors from the RC surface to space, the atmosphere and earth, respectively, the integral $\oiint dA_{RC}$ is carried out over the surface area of the RC, θ is the zenith angle, ϕ is azimuthal angle, T is temperature, ε is the emittance, C_g is the geometric solar concentration factor, h is the convection coefficient, and I_{BB} is the blackbody radiation, obtained from Planck's law.

$$I_{BB}(T,\lambda) = \frac{2h_p c^2}{\lambda^5} \frac{1}{e^{\frac{h_p c}{\lambda k_b T}} - 1} \tag{3-7}$$

where h_p is Planck's constant, k_b is the Boltzmann constant, and c is the speed of light in a vacuum. The RC surface is assumed to be diffuse and isothermal. ε_{RC} denotes the emittance of the RC. To simplify the analysis of radiative heat transfer between the RC and earth, earth surfaces are assumed to be black, diffuse and isothermal, therefore $\varepsilon_{earth}(\lambda, \theta) = 1$. An ideal blackbody is defined

as a surface that (1) absorbs and emits radiation with unit efficiency at all wavelengths and (2) behaves as a diffuse emitter, meaning that the intensity of emitted, absorbed, or reflected radiation is independent of direction. $\varepsilon_{atm}(\lambda, \theta)$ is the spectral directional atmospheric emittance. The relationship between $\varepsilon_{atm}(\lambda, \theta)$ and atmospheric transmittance $\tau_{atm,0}(\lambda)$ can be expressed as: [49]

$$\varepsilon_{atm}(\lambda, \theta) = 1 - \tau_{atm,0}(\lambda)^{\frac{1}{cos\theta}} \tag{3-8}$$

where ε_{atm} is the spectral directional atmospheric emittance and $\tau_{atm,0}$ is the spectral atmospheric transmittance in the normal direction. Notably, researchers often neglect the effects of atmospheric scattering and apply Equation (3-8) across all scenarios to simplify the analysis. However, as reported by Goody et al. [50] and Bennett et al. [51], the atmosphere exhibits significant scattering outside the 2 to 40 μm wavelength range, which cannot be ignored in those cases. In this study, the entire atmosphere from earth's surface to outer space is treated as a homogeneous, non-scattering medium. This simplification is justified because radiative heat transfer between the RC and atmosphere is only effective when both ε_{RC} and ε_{atm} are non-zero. As shown in Figure 3-2, the emittance spectra of both the broadband and selective RCs have non-zero values only within the 2–40 μm range. Within this spectral window, scattering effects in the atmosphere are negligible. Therefore, the atmosphere can be reasonably treated as a non-scattering medium in this study. The atmospheric temperature, which typically depends on the lapse rate, is replaced by the sea level temperature, assumed to be constant at all altitudes. The sea level transmittance, $\tau_{atm,0}(\lambda)$, is obtained from ATRAN [52]. The atmosphere is further simplified to be a hemispherical surface with a radius of one kilometer, with the center of the hemisphere at the same position as the center of RC and trough. The hemisphere is subdivided into a series of circular bands (which appear as surfaces resembling rings as shown on the right side of Figure 3-4) with zenith angular intervals

of 10° (or π/18 rad). Each ring is assumed to be diffuse, isothermal, and to have the properties of a black body. That is, within a band extending from δ to γ radians, all rays are assumed to have the same intensity as rays at the angle θ = (δ + γ)/2. The revised atmosphere emission intensity based on the angular intervals depicted in Figure 3-4 is as follows:

$$P_{atm,\delta-\gamma} = F_{RC-(atm,\delta-\gamma)} \oiint dA_{RC} \int_{\emptyset} \int_{\delta}^{\gamma} \sin\theta \cos\theta \int_{0}^{\infty} \varepsilon_{RC}(\lambda)\varepsilon_{atm}(\lambda,\theta) I_{BB}(T_{atm},\lambda) d\lambda d\theta d\emptyset \quad (3\text{-}9)$$

Furthermore, global solar irradiation is composed of direct and diffused irradiation. A correlation between direct and global solar irradiation is presented by Orgill et. al [53]. Their correlation between direct and global solar irradiation allows the estimation that, under clear and dry daytime conditions, approximately 82.3% of global irradiation is direct and 17.7% is diffuse.

3.2.3. Monte Carlo Ray Tracing (MCRT) Analysis

A Monte Carlo Ray Tracing (MCRT) code was developed to calculate $P_{cooling}$ for Cases 1 to 6 and the method used to relate the traced rays to radiative heat transfer is illustrated in Figure 3-4. To ensure the accuracy of the MCRT methodology, the number of diffuse rays was varied from one million to 20 million for Case 6 (with f = 0.016, H = 0.625, L = 1 m). It was found that $P_{cooling}$ changed by less than 0.01% when the number of rays was varied from 10 million to 20 million. Hence, 10 million rays were employed for all MCRT simulations. To evaluate when the emitter can be approximated as a line source, $P_{cooling}$ is computed for Case 6 when the diameter of the tubular RC is set to 1 mm, 0.1 mm and 0.01 mm. The results for $P_{cooling}$ changed by less than 0.01% when the diameter was decreased from 0.1 mm to 0.01 mm. Therefore, the line source emitter simulations were carried out assuming the RC had a diameter of 0.1mm. Two scenarios (i.e., a

perfectly diffuse broadband (ε =1 from 4–40 μm) or selective (ε =1 from 8–13 μm) emitter) are considered for the RC material (see Figure 3-2). The reflective surfaces (either flat for Cases 2 and 3 or in the shape of a parabolic trough for Cases 4 to 6) are assumed to be perfect specular reflectors that do not exhibit any absorption losses. Fictitious surfaces are used to model the radiative exchange between the emitter and outer space as well as the emitter and earth. These fictitious surfaces (e.g., at the top of the trough and the two side surfaces, as shown in Figure 3-4), are assumed to have both their emittance and absorptance to be equal to 1 for all wavelengths. The MCRT code is configured such that all rays are emitted from the RC surface. The MCRT code traces rays generated from random points on the RC with random zenith (θ) and azimuthal (ϕ) angles until they are absorbed by either a fictitious surface or the RC itself.

The rays emitted by the RC surface and intercepted by fictitious surfaces are classified based on whether they represent radiation that propagates into outer space or radiation absorbed by earth. This classification is based on the z-component of the ray direction vector at the point where the ray is intercepted by a fictitious surface, where a positive value indicates propagation toward space, and a negative value indicates propagation toward the earth. As shown in Figure 3-4, θ_{int} is the angle between the ray propagation direction vector and the positive z-axis at the point of interception with a fictitious surface. The calculation of θ_{int} is provided by Equation (3-10) and the value of θ_{int} for each ray is recorded.

$$\theta_{int} = \cos^{-1}\left(\frac{\boldsymbol{Z}\cdot\mathbf{R}}{|\boldsymbol{Z}||\boldsymbol{R}|}\right) \tag{3-10}$$

where **Z** is the z-axis vector and **R** is the ray's propagating directional vector.

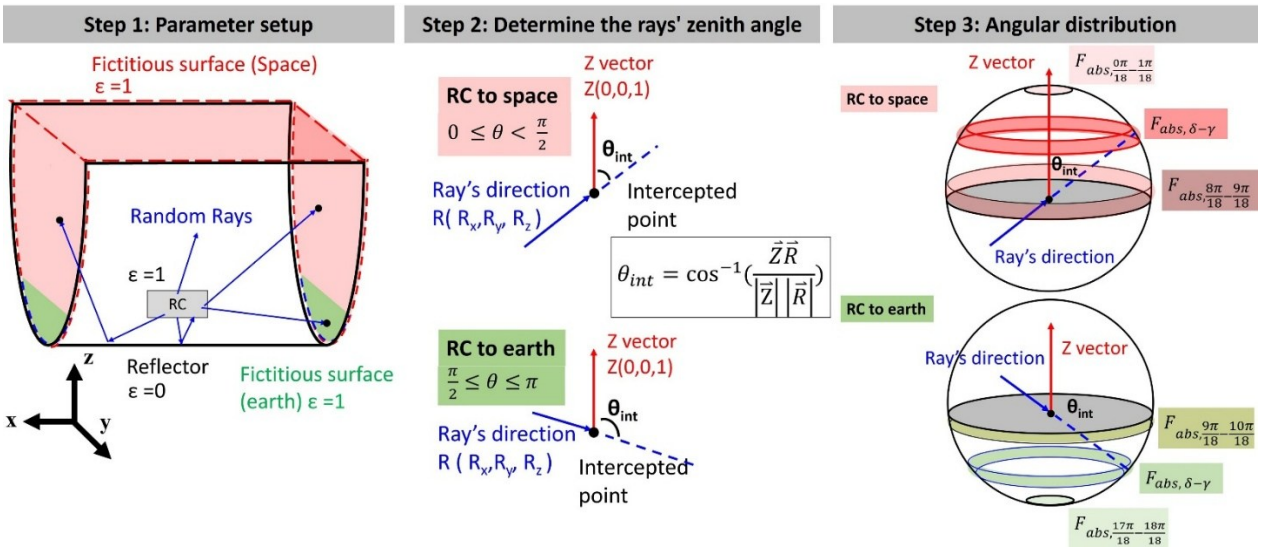

Figure 3-4: Partitioning of surfaces and methods for implementing the MCRT process

For Case 1, rays emitted from the RC with a zenith angle ranging from 0 to π/2 (from the z-axis to the x-y plane) propagate to outer space. In contrast, for π/2 < θ <π, the emitted rays are incident onto the underside blackbody. As a result, P_{RC} can easily be divided into two distinct components.

$$P_{RC} = P_{RC-space} + P_{RC-earth} \tag{3-11}$$

where $P_{RC\text{-}space}$ represents the radiation emitted from the RC directly towards outer space, and $P_{RC\text{-}earth}$ denotes the radiant energy emitted from the RC structure towards the earth. These two components can be calculated using Equations (3-13) and (3-13) as follows:

$$P_{RC-space} = \oiint dA_{RC}\left\{F_{abs,\frac{0\pi}{18}-\frac{1\pi}{18}} + F_{abs,\frac{1\pi}{18}-\frac{2\pi}{18}} \ldots + F_{abs,\frac{8\pi}{18}-\frac{9\pi}{18}}\right\}\int_{\emptyset}\int_{0}^{\infty}\varepsilon_{RC}(\lambda)I_{BB}(T_{RC},\lambda)d\lambda d\emptyset \tag{3-12}$$

$$P_{RC-earth} = \oiint dA_{RC}\left\{F_{abs,\frac{9\pi}{18}-\frac{10\pi}{18}} + F_{abs,\frac{10\pi}{18}-\frac{11\pi}{18}} \ldots + F_{abs,\frac{17\pi}{18}-\frac{18\pi}{18}}\right\}\int_{\emptyset}\int_{0}^{\infty}\varepsilon_{RC}(\lambda)I_{BB}(T_{RC},\lambda)d\lambda d\emptyset \tag{3-13}$$

where $F_{abs,\delta\text{-}\gamma}$ are the fraction of rays emitted from the RC with θ between δ rad to γ rad. The $F_{abs,\delta\text{-}\gamma}$ values are determined using the results from the MCRT simulations.

Moreover, using the reverse Monte Carlo ray tracing method, the incoming radiative power from earth (P_{earth}) and the atmosphere (P_{atm}) can be determined using the $F_{abs,\delta-\gamma}$ values. To simplify the reverse Monte Carlo ray tracing of incoming atmospheric radiation, the circular bands on the hemispherical surface representing the atmosphere, which extend from δ to γ (see the right side of Figure 3-4), can be treated as a series of blackbodies.

By the reciprocity theorem, the exchange fraction from each δ–γ band on the hemispherical surface representing the atmosphere to the RC emitter can be calculated using Equation (3-14). Consequently, $P_{atm,\delta-\gamma}$ can be expressed as shown in Equation (3-15). The total atmospheric radiation received by the RC can then be written as the sum of the radiation received from each δ-γ band as shown in Equation (3-16).

$$F_{(atm,\delta-\gamma)\ -RC} = \frac{\oiint dA_{RC}}{\oiint dA_{atm,\delta-\gamma}} \cdot F_{abs,\delta-\gamma} \tag{3-14}$$

$$P_{atm,\delta-\gamma} = \oiint dA_{atm,\delta-\gamma} \cdot \{\frac{\oiint dA_{RC}}{\oiint dA_{atm,\delta-\gamma}} \cdot \int_{\emptyset}\int_{0}^{\infty} F_{abs,\delta-\gamma} \cdot \varepsilon_{atm,\delta-\gamma}(\lambda,\theta) I_{BB}(T_{atm,0},\lambda) d\lambda d\emptyset\} \tag{3-15}$$

$$\begin{aligned} P_{atm} = \oiint dA_{RC} \{ & F_{abs,\frac{0\pi}{18}-\frac{1\pi}{18}} \int_{\emptyset}\int_{0}^{\infty} \varepsilon_{RC}(\lambda)\varepsilon_{atm}\left(\lambda,\frac{0.5\pi}{18}\right) I_{BB}(T_{atm,0},\lambda) d\lambda d\emptyset \\ & + F_{abs,\frac{1\pi}{18}-\frac{2\pi}{18}} \int_{\emptyset}\int_{0}^{\infty} \varepsilon_{RC}(\lambda)\varepsilon_{atm}\left(\lambda,\frac{1.5\pi}{18}\right) I_{BB}(T_{atm,0},\lambda) d\lambda d\emptyset \ldots \\ & + F_{abs,\frac{8\pi}{18}-\frac{9\pi}{18}} \int_{\emptyset}\int_{0}^{\infty} \varepsilon_{RC}(\lambda)\varepsilon_{atm}\left(\lambda,\frac{8.5\pi}{18}\right) I_{BB}(T_{atm,0},\lambda) d\lambda d\emptyset\} \end{aligned} \tag{3-16}$$

where $T_{atm,0}$ is the sea-level temperature of the atmosphere, and the integral $\oiint dA_{RC}$ is carried out over the surface area of the RC. $\oiint dA_{atm,\delta-\gamma}$ represents the emitted surface area over δ-γ band on the hemispherical atmospheric. With the same method, the total radiation coming from earth can be determined using Equation (3-17).

$$P_{earth} = \oiint \mathrm{dA}_{RC} \left\{ F_{abs,\frac{9\pi}{18}-\frac{10\pi}{18}} + F_{abs,\frac{10\pi}{18}-\frac{11\pi}{18}} \ldots + F_{abs,\frac{17\pi}{18}-\frac{18\pi}{18}} \right\} \int_{\emptyset} \int_{0}^{\infty} \varepsilon_{RC}(\lambda) I_{BB}(T_{earth}, \lambda) d\lambda d\emptyset \quad (3\text{-}17)$$

For Case 2, with the tubular RC positioned above a flat perfect reflector with an infinite area, the view factor from the RC to the atmosphere is doubled (when neglecting self-absorption by the RC) due to the reflection of radiation emitted in the downwards direction. That is, $P_{RC\text{-}earth}$ is specularly reflected toward outer space, and P_{earth} is equal to zero. Additionally, incoming radiation from the atmosphere (P_{atm}) and from the sun (P_{solar}) are also specularly reflected and according to the reciprocity theorem, the quantities P_{atm} and P_{solar} are doubled when absorbed by both the upper and underside of the RC surface. Therefore, the net cooling power for Case 2 is calculated using Equation (3-18):

$$P_{cooling} = 2 \cdot P_{RC-space}(T_{RC}) - 2 \cdot P_{atm}(T_{atm}) - 2 \cdot P_{solar} - 2 \cdot P_{nonrad}(T_{RC}, T_{atm}) \quad (3\text{-}18)$$

In Case 3, the RC is positioned above a flat square-shaped perfect reflector with a side length of 1 m, which resides on a blackbody surface of infinite size. Similarly, in Cases 4 to 6, the RC is placed such that its central axis aligns with the focal line of parabolic troughs that are situated above blackbody surfaces, which extend infinitely in the planar direction. The series of angular distribution factors for the emitted rays, $F_{abs,\,\delta\text{-}\gamma}$, is determined using MCRT. The radiative power components $P_{RC\text{-}space}$, $P_{RC\text{-}earth}$, P_{atm} and P_{earth} are obtained using Equation (3-12), (3-13), (3-16) and (3-17), respectively.

3.3. Results

The results are presented in five sections. Section 3.3.1 provides a brief discussion about the sub-ambient cooling effect and cooling performance of the RC for Cases 1 to 6. Section 3.3.2 explains the impact of the geometrical factors on the RC performance. Section 3.3.3 discusses the effects of atmospheric radiation. Section 3.3.4 evaluates convective heat transfer and solar radiation on RC performance. Finally, practical material properties are incorporated to assess the real performance of the RCs in Section 3.3.5.

3.3.1. Steady-state Temperature

Figure 3-5 shows the cooling power versus RC temperature for the six RC configurations shown in Figure 3-1. The mono-facial flat RC is included for comparison. For the results shown in Figure 3-5a the RC emitter is modeled as a tubular source (with diameter of 0.1 mm and length of 10 mm - see Figure 3-1). The results are shown for two scenarios: (i) the thermal emittance of the RC is an ideal step-function broadband emitter; or (ii) the thermal emittance of the RC is an ideal top-hat selective emitter (see Figure 3-2). The results are calculated based on the assumption that the temperature of the atmosphere and that of the surrounding earth are 300 K. Moreover, it is assumed that there is no incident solar radiation and no convective heat losses to the surroundings. It can be observed that $P_{cooling}$ is negative at low temperatures because the RC is being heated by the atmosphere or earth. On the other hand, at higher temperatures, $P_{cooling}$ has large positive values for all cases. It is because the RC radiative emission exceeds the absorbed heat from the atmosphere and surroundings, in addition to the radiative cooling.

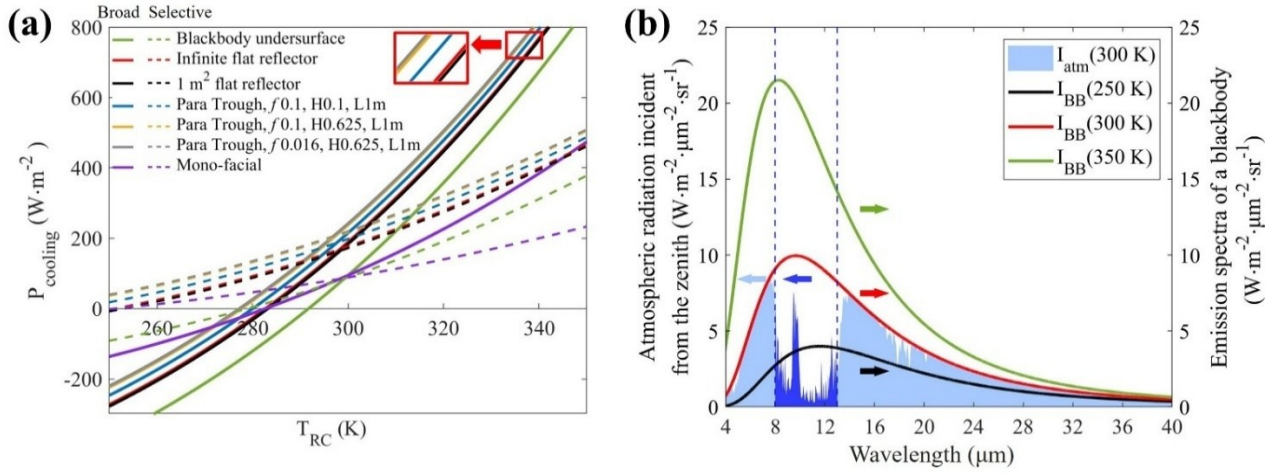

Figure 3-5: (a) The net cooling power ($P_{cooling}$) as a function of the temperature (T_{RC}) of the radiative cooler for the six configurations and a mono-facial case, evaluated for both the broadband (solid line) and ideal selective (dashed line) emittance spectra shown in Figure 3-2. The red box indicates magnified regions to better distinguish differences among the cases. (b) Comparisons of the atmospheric radiation incident from the zenith and the emission spectra from a blackbody at 250 K, 300 K, and 350 K. The area shaded in dark blue represents the atmospheric radiation absorbed for the case of the selective emitter, while the combined dark and light blue areas depict the total atmospheric radiation absorbed for the case of the broadband emitter.

Table 3-1**:** The steady-state temperatures ($T_{RC\text{-}ss}$) of the six radiative cooler configurations shown in Figure 3-1 compared to that of a mono-facial RC.

$T_{RC\text{-}ss}$	*Mono-facial*	*Case 1*	*Case 2*	*Case 3*	*Case 4*	*Case 5*	*Case 6*
Broadband	282.75 K	291.76 K	282.75 K	283.24 K	280.08 K	277.70 K	277.28 K
Ideal Selective	251.31 K	279.03 K	251.31 K	253.12 K	242.77 K	234.16 K	232.62 K

The RC reaches its steady-state temperature, $T_{RC\text{-}ss}$, when $P_{cooling} = 0$, and the corresponding values are listed in Table 3-1. Notably, all cases exhibit lower $T_{RC\text{-}ss}$ when the RC functions as a selective emitter compared to a broadband emitter. This is because, for steady-state temperature below the ambient atmospheric temperature ($T_{atm} = 300$ K), the net radiative transfer between the atmosphere

and the RC is in the direction from the atmosphere to the RC. For a selective emitter, radiative exchange with the atmosphere occurs only within the atmospheric window, resulting in a significantly lower P_{atm}. In contrast, broadband emitters experience increased P_{atm} due to radiative exchange over a broader spectral range, leading to a higher steady-state temperature of the RC, as shown in Figure 3-5b**.** The steady-state temperature ($T_{RC\text{-}ss}$) for the mono-facial RC is 282.75 K and 251.31 K when the RC is a broadband and selective emitter, respectively. When the emitter is bifacial and an underside blackbody surface is incorporated (Case 1), $T_{RC\text{-}ss}$ is 291.76 K and 279.03 K when the RC is a broadband and selective emitter, respectively. When a flat infinitely wide reflector is placed beneath the RC material (Case 2), $T_{RC\text{-}ss}$ decreases significantly from 291.76 K to 282.75 K when the RC is a broadband emitter and from 279.03 K to 251.31 K when the RC is a selective emitter. The results for Case 2 are the same as those for the mono-facial RC, as both the RC upward- and downward-facing surface exhibit the equivalent radiative interaction with space, the atmosphere and earth as the mono-facial RC (see Equation (3-18)).

In comparing $T_{RC\text{-}ss}$ for Cases 2 and 3, it can be noted that placing a flat reflector with a surface area of 1 m^2 beneath the RC (Case 3) enhances the cooling power nearly to the same extent as when an infinitely wide flat reflector is placed beneath the RC (Case 2). The difference in $T_{RC\text{-}ss}$ for Cases 2 and 3 is less than 0.5 K for the broadband emitter and less than 1.8 K for the selective emitter. This is because Case 3 allows a small amount of radiative interaction between the RC and earth.

Comparing the results of Cases 3 and 4 highlights the impact of the parabolic trough reflector. In Case 3, rays reflected from the underside reflector experience a reversal of the z-component of their direction vector **R**. In contrast, in Case 4, reflections from the parabolic trough alter both the

z- and y-component of **R**, thereby redirecting radiation into different angular sectors. As a result, the values of the $F_{abs,\delta-\gamma}$ factors in Equation (3-12), (3-13), (3-16) and (3-17) differ significantly between the two cases. This angular redistribution decreases the F_{abs} factors with higher values of δ and γ and increases the number of rays propagating towards outer space at lower zenith angles. Considering the reciprocity theorem, since the intensity of the incident radiation from the atmosphere is lower at small zenith angles, the angular redistribution imposed by the parabolic reflector results in a lower value of P_{atm}. This in turn results in improved radiative cooling performance. Specifically, the steady-state temperature drops from 283.24 K (Case 3) to 280.08 K (Case 4) for a broadband emitter and from 253.12 K to 242.77 K for a selective emitter.–

The difference in the cooling effects between Cases 4 and 5 is attributed to the trough height. In Case 4 (i.e., trough height = 0.1 m), the parabolic trough reflector affects radiative heat exchange only for rays emitted in downward directions. In contrast, in Case 5 the parabolic reflector (i.e., trough height = 0.625 m) influences radiative heat exchange for radiation emitted in the downward direction as well as a portion of the rays emitted in upwards directions. The deeper trough in Case 5 shifts a larger fraction of rays emitted at higher zenith angles to lower zenith angles as compared to Case 4, resulting in a further reduction of P_{atm} and an increased cooling effect.

A comparison between Cases 5 and 6 reveals Case 6, which has a smaller focal length and thereby a narrower trough, further enhances the cooling performance by reducing radiative interaction between the RC and earth while increasing the radiative exchange between RC and space.–

When comparing the steady-state temperatures, T_{RC-ss}, of parabolic troughs and paraboloid dishes [48] with identical focal lengths and heights, the dishes consistently yield lower T_{RC-ss}. For selective emitters in Case 4, where both the dish and trough have a focal length of 0.1 m and a

height of 0.1 m, $T_{RC\text{-}ss}$ is 234.7 K for the dish and 242.77 K for the trough. For Case 5, with a focal length of 0.1 m and a height of 0.625 m, the corresponding $T_{RC\text{-}ss}$ is 230.9 K for the dish and 234.2 K for the trough. For Case 6, with a focal length of 0.016 m and height of 0.625 m, $T_{RC\text{-}ss}$ is further reduced to 226.58 K for the dish and 232.62 K for the trough.

This phenomenon arises because the paraboloid dish redirects all the outgoing rays emitted from the bottom surface of the RC, as well as a portion of those emitted from the top surface, into upward directions with lower zenith angles through two-dimensional parabolic reflection. After reflection by the dish, only the atmospheric radiation from directions with small zenith angles can reach the bottom surface of the RC, moreover, atmospheric radiation from large zenith angles is effectively blocked from reaching the top surface, as well. For example, for a paraboloid dish reflector with focal length and height similar to that of Case 6, approximately 96.7% of the rays emitted from the RC propagate into outer space with a zenith angle confined to within 0 to $\pi/18$ radians. In contrast, for the parabolic trough reflectors (Cases 4 to 6), the corresponding fraction within 0 to $\pi/18$ radians drops to 4.5%, 9.9% and 13.4%, respectively. Unlike the dish, the parabolic trough redirects rays only in one dimension, leaving the RC exposed to radiation at large zenith angles, both from the atmosphere and ground, through its lateral openings. Although this geometric limitation reduces the overall cooling performance, the trough design offers a practical advantage in industrial applications. In particular, it allows fluid to pass along the focal line, which is not feasible in dish-type configurations.

3.3.2. Effect of Trough and Emitter Geometry

This section investigates the effects of the trough and emitter geometries on the RC cooling performance. In this section P_{solar} and P_{nonrad} are neglected to simplify the analysis. The temperature of the atmosphere, earth, and the RC surface are set to 300 K. Figure 3-6 illustrates the effect of the trough length and height on the net cooling power for broadband (Figure 3-6a) and selective (Figure 3-6b) emitters, respectively. For the results shown in Figure 3-6 the RC is in the form of a line with a diameter of 0.1 mm and length of 10 mm centered along the focal line of the trough reflector, which has a focal length of 0.1 m.

Figure 3-6c provides a detailed view along the dashed line labelled A–A in Figure 3-6a, illustrating the effect of trough length when its height is 0.625 m and its focal length is 0.1 m. As the trough length increases, a greater portion of the emitted rays are reflected and directed towards outer space, rather than being incident onto the ground. Additionally, the trough slightly reduces the fraction of rays that propagate to outer space at large zenith angles (dashed blue line), while increasing the number of rays that propagate to space at low zenith angles (dashed red line). The net cooling power increases rapidly as the trough length grows from 0 to 0.32 m and continues to rise at a slower rate beyond this point. $P_{cooling}$ shows negligible improvements with increasing trough length when the trough length exceeds 1 m, stabilizing at 236.87 $W \cdot m^{-2}$ for the broadband emitter and 215.52 $W \cdot m^{-2}$ for the selective emitter as the trough length approaches infinity.

Figure 3-6d provides a detailed view along the dashed line labelled as B–B in Figure 3-6a, illustrating the effect of trough height for a trough with a length of 1 m and focal length of 0.1 m. When the trough height is 0.1 m, even a slight increase leads to a significant enhancement in $P_{cooling}$. However, once the trough height exceeds approximately 0.3 m, the improvement in $P_{cooling}$ with

increasing trough height becomes more gradual and eventually negligible beyond a height of 0.625 m. This behavior arises because, at low trough heights, small increases in the trough height more effectively redirect rays from large zenith angles to directions with lower zenith angle, thereby reducing the absorbing atmospheric radiation.

Figure 3-6e compares a wider trough (f = 0.1 m) and a narrow trough (f = 0.016 m), with both troughs scaled such that their lengths and heights maintain the same ratio to their respective focal lengths. This comparison is used to examine the influence of focal length. The results show that when both the length-to-focal-length ratio and the height-to-focal-length ratio of the troughs are identical, the net cooling power remains nearly the same in both configurations. This indicates that the effect of trough geometry can be effectively characterized based on focal length scaling. Consequently, the results from Figure 3-6 suggest that the cooling power of trough-based and line type of RC systems can be more efficiently estimated using geometric scaling relative to the focal length.

Peoples et al. [39] reported the amplification factor of the cooling power that can be achieved by using an underside reflective V-shaped trough, compared to the mono-facial case, approaches a factor of 2 as the trough length becomes infinitely long. This calculation is based on the increase in the effective surface area of the emitter. However, the incorporation of parabolic trough reflectors can amplify the cooling power by more than a factor of two. The additional improvement is attributed to redirection of absorbed atmospheric radiation from high-air-mass directions (at higher zenith angles) to those with lower air mass (at lower zenith angles). For example, considering Case 5, the amplification factor reaches 2 as the trough length reaches 0.17 m (for a broadband emitter) and 0.19 m (for a selective emitter), and can be further increased to 2.53

(broadband) and 2.45 (selective) as both trough length and trough height approach infinity.

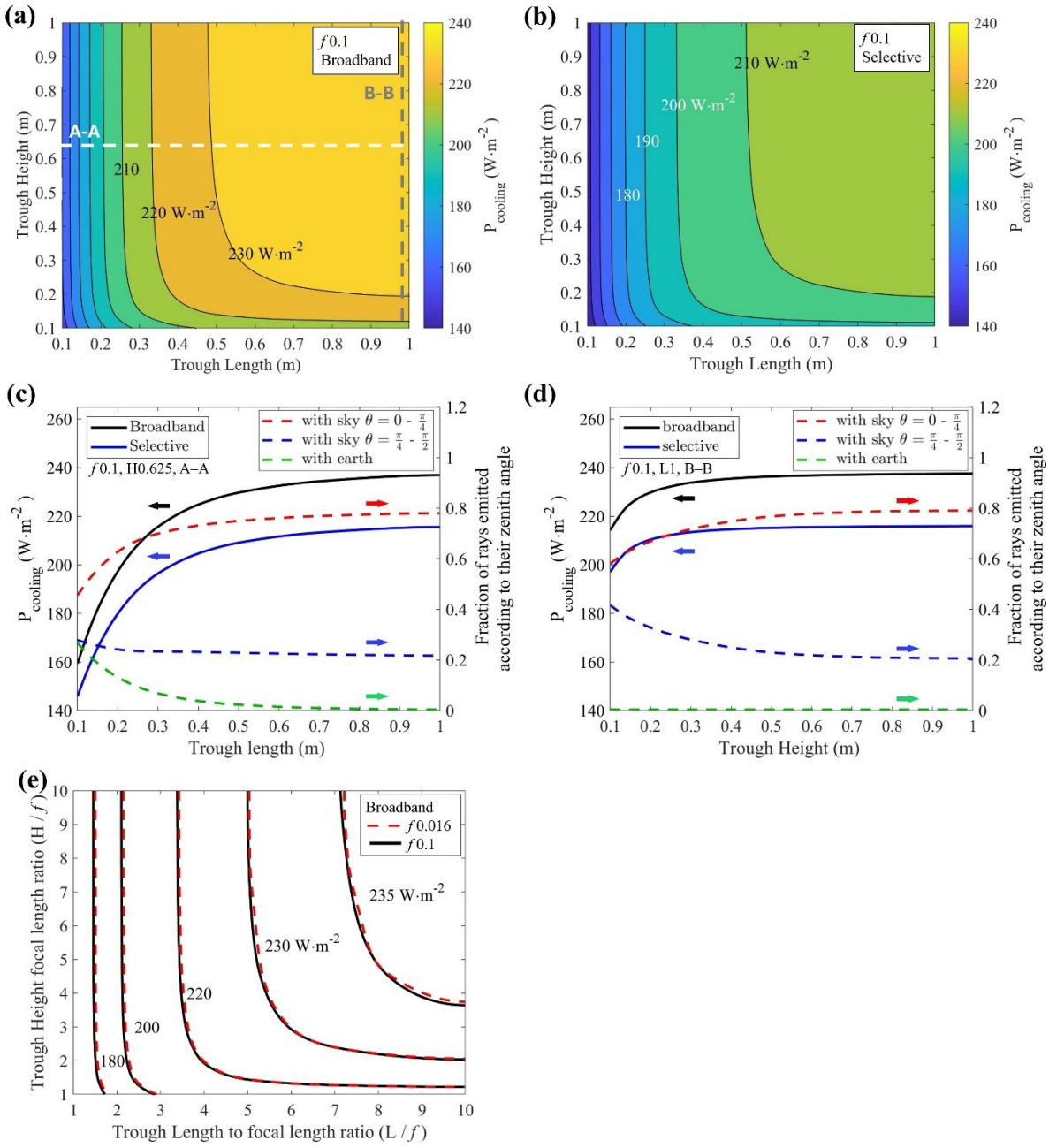

Figure 3-6: The net cooling power as a function of both trough length and trough height for (a) broadband emitter and (b) selective emitters in f 0.1 trough (c) Detailed view along the dashed line A–A in Figure 3-6a, illustrating the influence of trough length on the net cooling power of a fixed height of 0.625 m trough. (d) Detailed view along the dashed line B–B in Figure 3-6a, illustrating the influence of trough length on the net cooling power of a fixed length of 1 m trough. (e) Effect of focal length on net cooling power for troughs with equal height.

Dimensionless analysis was performed on the parabolic trough geometry (Case 5) to determine the impact of the normalized receiver parameters on net cooling power. The study varied the tubular RC-emitter-length-to-trough-length ratio (L_{RC}/f) and RC-diameter-to-focal-length ratio (D_{RC}/f). Results showing the net cooling power for broadband and selective emitters are illustrated in Figure 3-7a and Figure 3-7b, respectively. Notably, along the dashed line C–C and line D–D in Figure 3-7b, the tubular RC has the same horizontal projected area (length × diameter), yet they exhibit distinctly different values of $P_{cooling}$. This indicates that varying the RC length and diameter leads to distinct ray direction distributions, and consequently, different radiative interaction with outer space, the atmosphere and earth. Figure 3-7c provides a detailed view along the dashed line A–A in Figure 3-7a, illustrating the effect of increasing the RC length (with a fixed diameter of 0.1 m) in Case 5. When the RC is short, increasing its length initially enhances RC self-absorption, thereby reducing $P_{cooling}$. The self-absorption fraction ultimately converges to approximately 0.15. As the RC length approaches the trough length, the fraction of rays interacting radiatively with earth increases, further reducing $P_{cooling}$. The fraction of rays at large zenith angles remains nearly constant throughout. Figure 3-7d provides a detailed view along dashed line B–B in Figure 3-7a, illustrating the effect of RC diameter for a 0.1-meter-long RC in Case 5. $P_{cooling}$ is significantly reduced even when the RC does not approximate a line source ($D_{RC} \sim 0$), due to enhanced self-absorption. From Figure 3-7d $P_{cooling}$ decreases more rapidly with increasing diameter when the diameter is at higher values. The fraction of rays at large zenith angles remains largely unchanged. Additionally, the fraction of rays interacting with earth is inherently negligible since the trough length is sufficiently long relative to the RC.

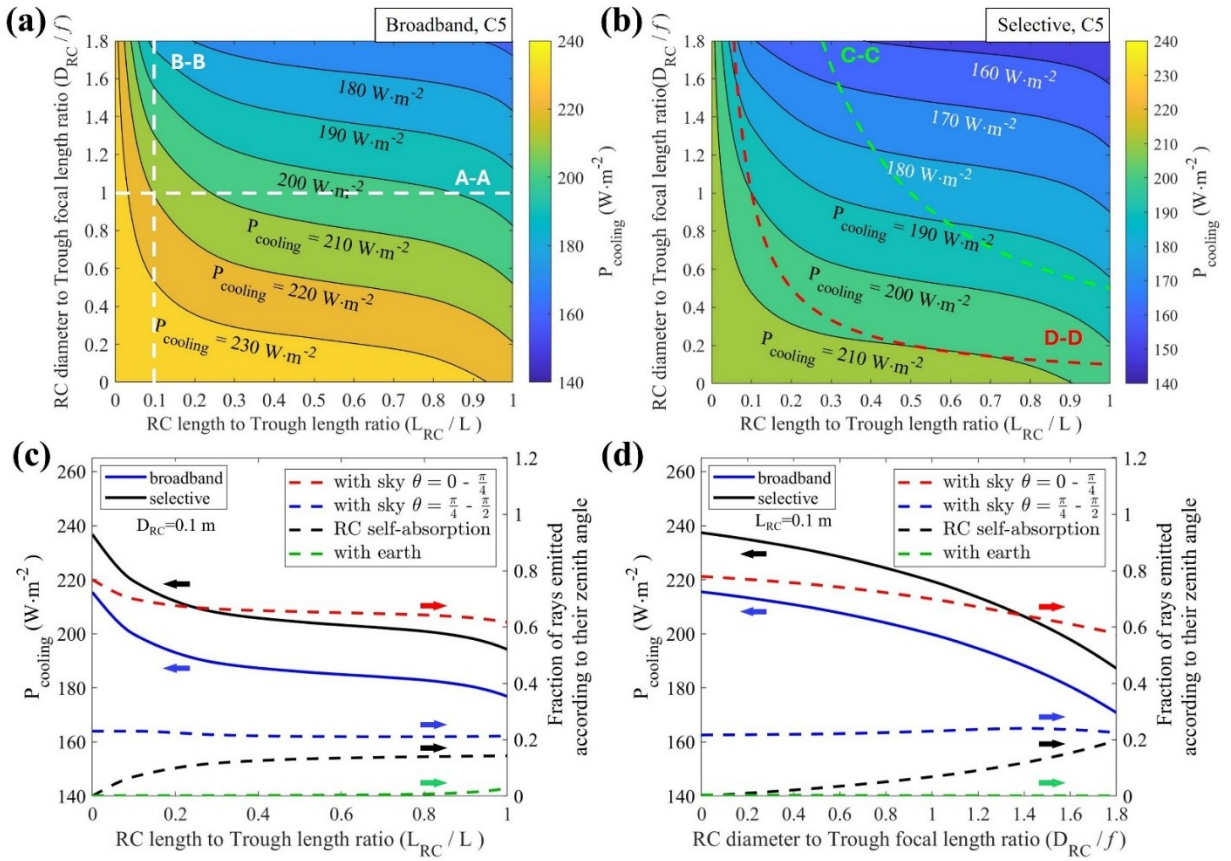

Figure 3-7:. The effects of RC length and its diameter for the Case 5 trough on the net cooling power. (a) broadband emitter (b) selective emitter. (c) Detailed view along the dashed line A–A in Figure 3-7a, illustrating the influence of RC length on the net cooling power (d) Detailed view along the dashed line B–B in Figure 3-7a, illustrating the influence of RC diameter on the net cooling power.

3.3.3. Effects of Atmospheric Radiation on Cooling Performance

Three primary factors influence the amount of atmospheric radiation absorbed by the RC surface: atmospheric emittance (ε_{atm}), the atmospheric temperature (T_{atm}) and the RC emittance (ε_{RC}). Among these, atmospheric emittance is strongly dependent on the air-mass, as discussed in the Method section. Figure 3-8a illustrates the effects of absorbed atmospheric radiation, governed by T_{atm}, on the steady-state temperature of the RC surface, where P_{solar} and P_{nonrad} are neglected to

isolate the influence of atmospheric radiation.

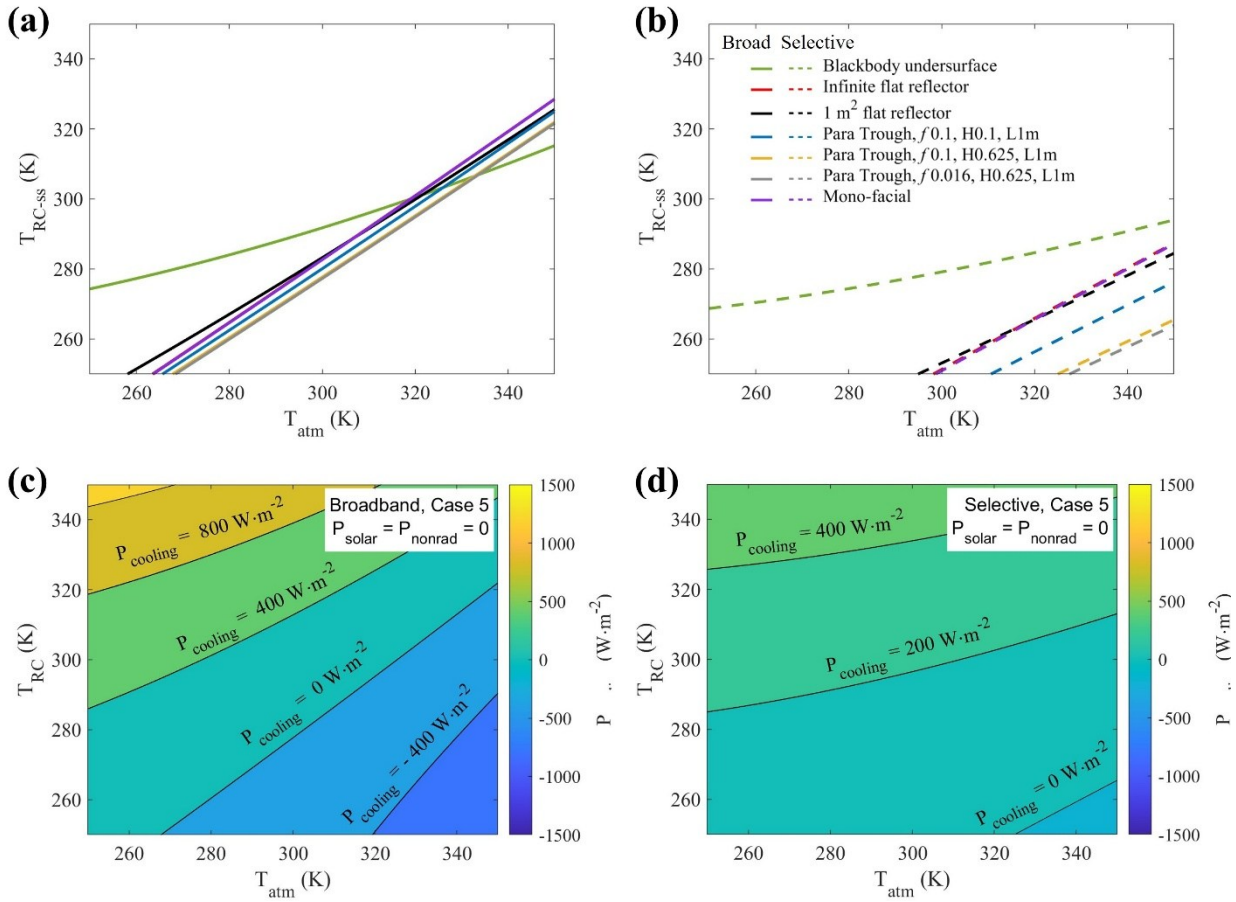

Figure 3-8**:** (a, b) T_{RC-ss} plotted as a function of T_{atm} for (a) a broadband emitter and (b) a selective emitter. (c, d) $P_{cooling}$ as functions of T_{atm} and T_{RC} for Case 5 (*f* 0.1, H0.625, L1) with a (c) broadband emitter and (d) selective emitter.

In Figure 3-8a and Figure 3-8b, the area to the left of each contour line indicates regions where the cooling power is positive, while the area to the right-side shows conditions where the cooling power is negative. The results show that across all six cases, the steady-state RC temperature (T_{RC-ss}) is slightly lower than T_{atm}, indicating a sub-ambient cooling effect. Notably, Case 1 (underside blackbody) exhibits a different contour pattern compared to the other cases, as atmospheric radiation only influences the sky-facing surface of the RC, whereas the downward-facing surface is affected by radiation from the earth which is held at a constant value of T_{earth} = 300 K in this

analysis. Furthermore, Case 2 (infinite flat reflector) yields results identical to the Mono-facial reference case, as previously discussed. Figure 3-8c and Figure 3-8d present the cooling power of a broadband emitter and a selective emitter, respectively, with a RC diameter of 0.1 mm and length of 10 mm (line-source emitter) for the parabolic trough from Case 5, as a function of T_{atm} and T_{RC}. The third factor is RC emittance, which is assumed to be isotropic. In this analysis $\varepsilon_{RC} = 1$ from 4 $-$40 μm for the broadband emitter and from 8$-$13 μm for the selective emitter, while $\varepsilon_{RC} = 0$ outside these ranges. When ε_{RC} is varied, P_{RC}, P_{atm} and P_{earth} exhibit a linear proportionality to ε_{RC} as described by Equation (3-12), (3-13), (3-16) and (3-17).

3.3.4. Effects of convective heat transfer and solar radiation on cooling power

In the previous sections P_{nonrad} and P_{solar} were assumed to be zero in order to isolate and analyze the effects of the geometry and incident atmospheric radiation on $P_{cooling}$. This section investigates the influence of environmental heat exchange (P_{nonrad}) and absorbed solar radiation (P_{solar}) on the RC cooling power. The analysis includes Cases 1 through 5 as defined in Figure 3-1, assuming a fixed tubular RC diameter of 0.1 m and a length of 0.01 m. Case 6 is also included, designed to maintain the same RC diameter-to-focal length ratio as Case 5. The corresponding RC diameter is 0.016 m and the length is 0.01 m in Case 6. The associated geometric solar concentration ratios (C_g) are 1.3, 3.2 and 8 for Case 4 through Case 6, respectively.

3.3.4.1. Effect of Convective Heat Transfer

The steady state temperature of the RC, $T_{RC\text{-}ss}$, is plotted as a function of the convective heat transfer coefficient in Figure 3-9, assuming an ambient temperature of 300 K and $P_{solar} = 0$. To capture the convective conditions relevant to low-wind operation, the analysis adopts a range of convection coefficients between 0 and 20 W m^{-2} K^{-1}. According to the Beaufort wind scale [54], 'light air' conditions correspond to a wind speed of approximately 5 km/h, which yields a convection coefficient of about 22.2 W m^{-2} K^{-1} based on the Churchill–Bernstein equation for crossflow over a cylindrical surface. Therefore, the selected range (0–20 W m^{-2} K^{-1}) encompasses the convective regime expected under calm to light-air environmental conditions, where radiative cooling performance is most relevant.

As shown in Figure 3-9a and Figure 3-9b, when the convection coefficient *h* increases from 0 to 5 $W \cdot m^{-2} \cdot K^{-1}$, the sub-ambient cooling effect deteriorates rapidly for both the broadband and selective RC across all six cases. As *h* continues to increase to of 20 $W \cdot m^{-2} \cdot K^{-1}$, $T_{RC\text{-}ss}$ gradually approaches the ambient temperature, T_{atm}. This trend indicates that convective (non-radiative) heat transfer becomes a dominant mechanism offsetting the sub-ambient cooling, particularly when a temperature gradient exists between the RC and the atmosphere. Figure 3-9c and Figure 3-9d present the cooling power of the RC for the broadband and selective reflectors, respectively, as functions of both the RC temperature and the convective heat transfer coefficient. For these analyses, the RC is modeled with a diameter of 0.016 m and length of 0.01 m, positioned along the focal line of a parabolic trough with a focal length of 0.016 m, a height of 0.625 m, and a length of 1 m (Case 6).

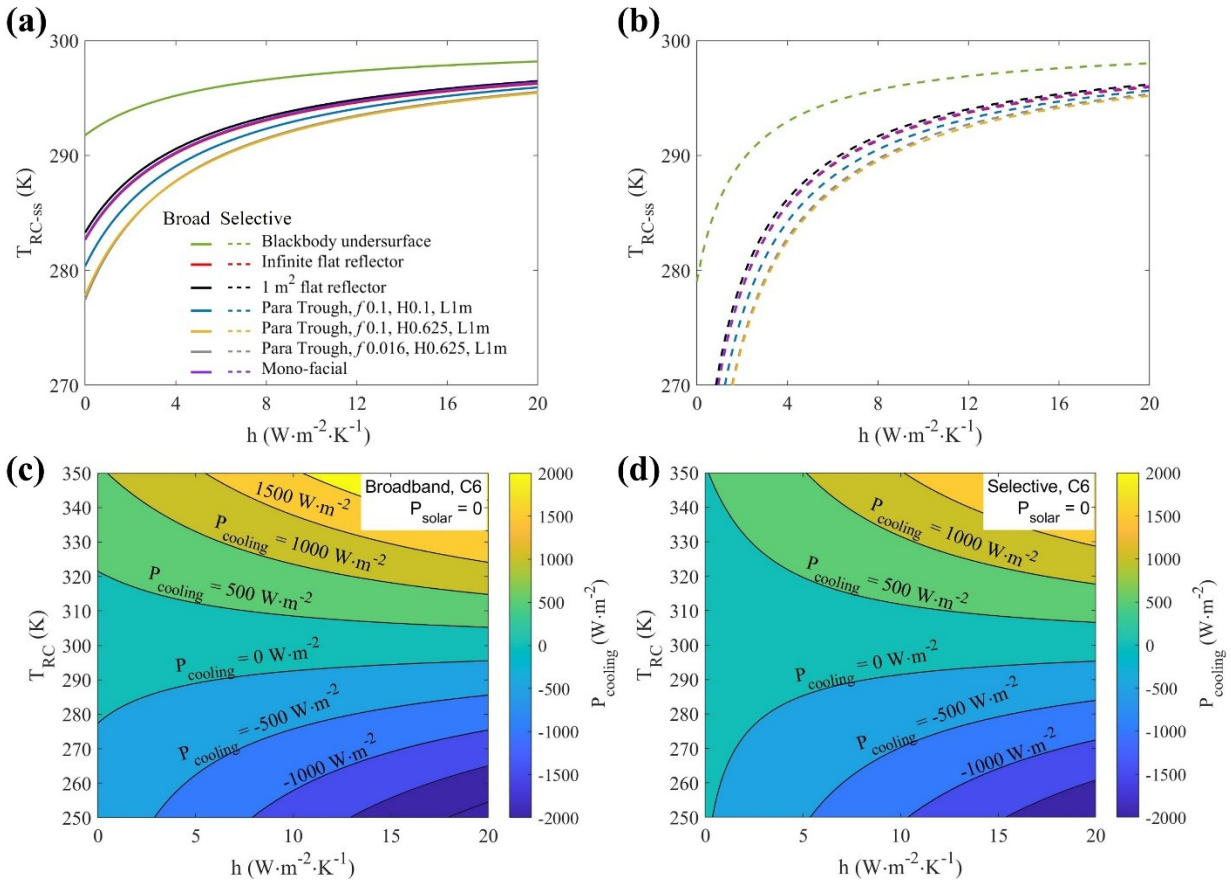

Figure 3-9: **(a, b)** Steady-state temperature of the RC as a function of the convection coefficient *h* for (a) a broadband emitter and (b) a selective emitter. **(c, d)** Cooling power of the RC as functions of *h* and RC temperature for Case 6 (*f* 0.016, H0.625, L1), shown for **(c)** a broadband emitter and **(d)** a selective emitter.

3.3.4.2. Effect of Solar Radiation

In this analysis the global solar radiation is assumed to be 1000 $W \cdot m^{-2}$, consisting of 823 $W \cdot m^{-2}$ direct and 177 $W \cdot m^{-2}$ diffuse components [53]. The geometric concentration ratio (C_g) is 1.3, 3.2 and 8 for Case 4 to Case 6, respectively. The ambient temperature is set at 300 K, and non-radiative heat transfer is neglected. Figure 3-10a illustrates the effective region of incoming direct solar radiation for Case 5 and Case 6 as functions of solar altitude and azimuth angles. The focal length

of the trough is aligned along the 0˚–180˚ direction. In the polar plot, the azimuthal angle corresponds to the solar azimuth, and the radial distance represents the solar altitude angle. Although Case 6 has a higher geometric concentration ratio (8) than Case 5 (3.2), its effective region of incoming direct solar radiation is significantly smaller. This indicates that the narrower trough (Case 6) is more effective at blocking direct solar radiation, thereby reducing the impact of concentrated solar input. The blue shaded area represents the acceptance angle ($2\theta_s$=14.4˚) of Case 6, which corresponds to a geometric solar concentration ratio of 8. Figure 3-10a offers valuable insight for optimizing trough orientation based on site-specific solar angels, enabling location-adaptive system design.

Figure 3-10b shows the influence of absorbed solar radiation on the net cooling power. For Case 5, sub-ambient cooling is entirely negated when the absorbed solar radiation reaches 234.4 $W \cdot m^{-2}$ for the broadband emitter and 213.8 $W \cdot m^{-2}$ for the selective emitter. For Case 6, the corresponding threshold values are 228.4 $W \cdot m^{-2}$ (broadband) and 207.8 $W \cdot m^{-2}$ (selective). When the sun is directly overhead, sub-ambient cooling will not occur when the solar absorptance reaches 7.8 % and 7.2 % for the broadband and selective emitters in Case 5, respectively; and 3.3 % and 3.0 % in Case 6. These numbers are so low because the incoming solar radiation on the RC surface is magnified to 2797 W/m^2 and 6726 W/m^2 by trough reflection for Case 5 and Case 6, respectively. When the direct solar radiation is fully blocked, only diffuse solar radiation is effective, which is not concentrated by trough. The sub-ambient cooling can still be achieved even at higher solar absorption—up to 66.2 % (broadband) and 60.4% (selective) for Case 5, and 64.5 % (broadband) and 58.7 % (selective) for Case 6.

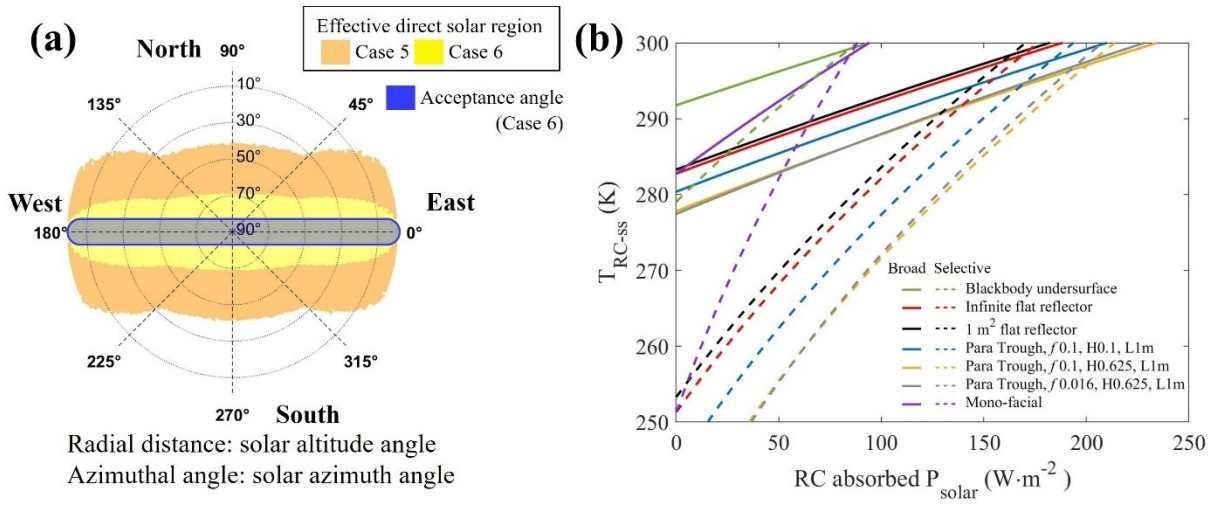

Figure 3-10(a) The effective regions of incoming direct solar radiation for Case 5 and Case 6 as functions of solar attitude and azimuth angles. (b) The RC steady-state temperature as a function of absorbed solar radiation.

3.3.5. Assessment of the performance for an RC material

The RC cooling performance and sub-ambient temperature drop were further evaluated using the properties of a hierarchically porous PVDF-HFP film emitter proposed by Pirvaram et al.[23]. This material was selected due to its high average emittance of 0.985 across the atmospheric window and high solar reflectance of 0.982. The simulation results show that a 1-cm-long tubular RC with a diameter equal to the configured trough—0.1 m for Case 5 and 0.016 m for Case 6—operating at an ambient temperature of 300 K, without convective heat transfer and exposed only to 286.9 $W \cdot m^{-2}$ of diffuse solar radiation, can achieve sub-ambient temperature of 237 K and 235.9 K when integrated with Case 5 and Case 6 configurations, respectively. Furthermore, when a convective heat transfer coefficient of 5 $W \cdot m^{-2} \cdot K^{-1}$ is considered, the corresponding steady-state temperatures are 285.8 K for Case 5 and 285.2 K for Case 6.

3.4. Conclusion

In summary, this study investigates the net cooling performance of a three-dimensional radiative cooling (RC) structure, considering various underlying reflector configurations and non-reflector cases. The analysis includes two types of emittance spectra: broadband and selective emitters. It is demonstrated that integrating a parabolic trough significantly enhances cooling performance by (i) bifacially increasing the RC's effective radiating area and (ii) blocking radiation incident from large zenith angles, and (iii) serving as a solar shade to suppress the absorbed solar radiation. As both the trough length and height approach infinity the cooling power enhancement approaches 2.53-fold (broadband) and 2.45-fold (selective) compared to a flat mono-facial RC, when the RC exhibits a perfect solar reflectance. The study indicates that a geometric scaling based on focal length remains valid for line-type RCs, while tubular RCs exhibit deviations. Moreover, the analysis of trough effectiveness under varying solar angles provides valuable insight for location-specific and adaptive system design. Finally, the performance of a practical hierarchically porous PVDF-HFP film emitter is evaluated. The results confirm the potential for RC with underlying parabolic trough reflectors to achieve substantial sub-ambient cooling, demonstrating feasibility for integration into building rooftops, HVAC systems and off-grid cooling applications.

Chapter 4–Fabrication, Experimental Setup, and Performance Evaluation of RC Systems

4.1. Introduction

Phase inversion is a well-established technique for fabricating polymer membranes, in which a polymer solution undergoes a controlled transformation from the liquid phase to the solid phase. In this process, the polymer is dissolved in a mixed solvent–non-solvent system. Owing to the high volatility of the solvent, evaporation increases the relative concentration of both the polymer and the non-solvent. This compositional shift induces polymer to precipitation, ultimately resulting in the formation of a skinned membrane [55]. Among the governing parameters, the solvent evaporation rate plays a decisive role in determining the resulting porous morphology. Previous studies have shown slow evaporation tends to generate cellular morphologies (e.g., closed-cell or open-cell), whereas rapid evaporation produces granular or unconnected morphologies, as reported by Kimmerle and Strathmann et al [56]. Another critical factor is the roughness of the casting substrate, which strongly influences membrane shrinkage behavior. When the polymer solution is cast on woven or nonwoven substrates, shrinkage is largely restricted to thickness direction, leading to the formation of larger pores due to inhibited lateral contraction. Conversely, casting on smooth substrates permits two-dimensional shrinkage, which reduces lateral dimensions, as demonstrated by Finken [57], [58].

Poly(vinylidene fluoride-co-hexafluoropropylene) (PVDF-HFP) has recently attracted increasing attention owing to its intrinsic dielectric and optical properties [26], [57], [58], which render it particularly suitable for passive daytime radiative cooling (PDRC) applications. PVDF-HFP membranes not only exhibit negligible extinction coefficient in the solar spectrum (0.3–2.5 μm) but also display multiple extinction peaks in the thermal infrared region (4–20 μm), enabling a combination of high solar reflectance and strong atmospheric window emittance. Mandel et al. demonstrated that the formation of open micro- and nano-porous structure significantly enhances the solar backscattering, while a hierarchical morphology consisting of the micro-pores coated with nano-pores facilitates a gradual refractive index transition across polymer-air interface. This gradient reduces optical impedance mismatch and promotes efficient long-wave infrared emission. Building on this, Pirvaram et al [24]. reported optimized PVDF-HFP films exhibiting solar reflectance of 0.982 and emittance of 0.985 within atmospheric transparency window. Their work attributed this performance to carefully tailoring polymer–solvent–nonsolvent composition, particularly through adjustment of the non-solvent (water) content. The optimized mass ratio of polymer-solvent-nonsolvent (1:8:1.25) identified in their study is adopted in present work for fabrication of RC emitter.

The integration of reflective geometries with radiative cooling surfaces has been increasingly investigated as an effective approach to enhance daytime cooling performance. In particular, parabolic trough reflectors [45], [46], [47], [48] and paraboloid dish reflectors [49] have been demonstrated to improve thermal radiation extraction and suppress parasitic solar heating. The primary function of the parabolic reflector is to redirect the otherwise diffuse thermal emission from the RC surface toward the open sky at near-vertical zenith angles, thereby increasing the probability of radiation transmission through the shortest air path.

Pirvaram et al. [48] conducted a numerical study in which bifacial RC emitters were combined with paraboloid dish reflectors. Their results indicated that such a configuration significantly enhances the effective radiative surface area and minimizes the emission zenith angle, leading to a reported sub-ambient cooling of up to 10 °C. Complementarily, Dan et al. [44] demonstrated the use of a parabolic trough reflector tiled 15° toward the anti-sunward direction, effectively shielding the RC surface from the direct solar radiation. Their experimental results showed that this configuration achieved an average daytime cooling power of 121.29 W/m^2 compared to a horizontally oriented module.

Although the use of parabolic reflectors has shown promise in enhancing the cooling efficiency of radiative cooling (RC) system, several research gaps remain unaddressed. First, the integration of trough-based RC systems with active cooling media, such as air or fluid flow, remains underexplored. The coupled heat transfer between the flowing medium and the radiative emitter, which could enable hybrid radiative-convective cooling, requires further experimental verification. Second, while numerical models have been proposed to predict enhanced cooling with parabolic or paraboloid reflectors, experimental validation under realistic outdoor conditions is still limited. Current models often assume idealized atmospheric transparency and isotropic sky radiation, leading to discrepancies between theoretical predictions and real-world performance.

Building upon these advances, the present study extends beyond polymer fabrication to investigate trough-assisted RC systems under realistic outdoor conditions. By combining optimized PVDF-HFP emitters with reflective parabolic geometries, this work aims to bridge material-level development with system-level validation, thereby providing a comprehensive framework for enhancing daytime radiative cooling performance.

4.2. Materials and Methods

4.2.1. Materials

Coated Materials: Poly(vinylidene fluoride-co-hexafluoropropylene) (PVDF-HFP, Sigma-Aldrich, CAS No. 9011-17-0) with a Mn of ~ 470,000 g/mol and a Mw of ~145,000 g/mol was used as the primary polymer in this study. PVDF-HFP pellets were utilized in all formulations. Deionized (DI) water and acetone (purity ≥ 99.9%) were employed as the nonsolvent and solvent, respectively. A double-sided thermal adhesive tape (Gdrtwwh, Gdrtwwh Inc.) with a thickness of 0.2 mm and an average thermal conductivity of 1.5 W/m·k was employed to bond the PVDF-HFP membrane to the substrate surface.

A nonreflective aluminum black foil tape (LLPT, NC233, thickness 0.2 mm) was used as the blackbody reference emitter. The material exhibits a total emittance of 0.94 in the UV-NIR range (0.3–2.5 μm) and maintains a value of 0.918 and 0.937 in the 8–13 μm (atmospheric window) and 4–20 μm bands, respectively.

Fluid Container: A copper pipe (Type M; Great Lakes Copper Inc.) with an inner diameter of 1.055 in, an outer diameter of 1.125 in, and a wall thickness of 0.035 in was used as the fluid substrate. The pipe ends were sealed with push-to-connect caps (SharkBite, 1 in), which were wrapped with fiberglass tape (ULINE, S-10514) to reduce heat loss.

4.2.2. Trough Configuration Setup

The trough configuration was constructed using 3D-printed parabolic channels, stainless steel L-beams and reflective aluminum sheets, with the channels serving to constrain the reflective aluminum sheet into a stable parabolic geometry within a square frame (Figure 4-1a). Edges 1 and 2 of the reflective sheets were inserted into the channels to a depth of 5 cm, while the other two edges were fixed onto stainless-steel L-beams to counteract deformation induced by the sheet's inherent spring force (Figure 4-1b). A reflective aluminum sheet (Anolux Miro-SILVER® 2000AG; Anomet Inc), with a total hemispherical reflectance of 0.97, was used as the reflective surface. A custom-designed constrain channel was fabricated from polylactic acid (PLA) using 3D printing to form the aluminum sheet into a parabolic trough. The PLA holder was secured within a square aluminum frame and reinforced with stainless-steel L-beams.

Both the tubular RC emitter and the blackbody reference emitter were positioned along the focal line of the trough using pipe holders mounted to the frame. Nine T-type thermocouples were deployed to monitor the thermal performance (Figure 4-1c). The external surface of the copper pipe was coated with the RC membrane and the pipe was filled with water. Plastic sheets were used to cover the two side openings of the trough, thereby reducing the influence of air convection on cooling performance.

In summary, two reflective parabolic troughs with a height of 0.15 m, a length of 0.56 m and a focal length of 0.1 m, each equipped with a tubular emitter containing approximately 0.407 kg of deionized water, were constructed to evaluate the performance of trough-enhanced radiative cooling.

For reference measurements, a testing structure without the parabolic reflector was employed (Figure 4-1d). In this configuration, both pipe emitters were clamped to a black-coated aluminum frame and positioned 5 cm above a blackbody flat surface (1 × 2 m), which was coated with the same black foil tape used for the blackbody emitter.

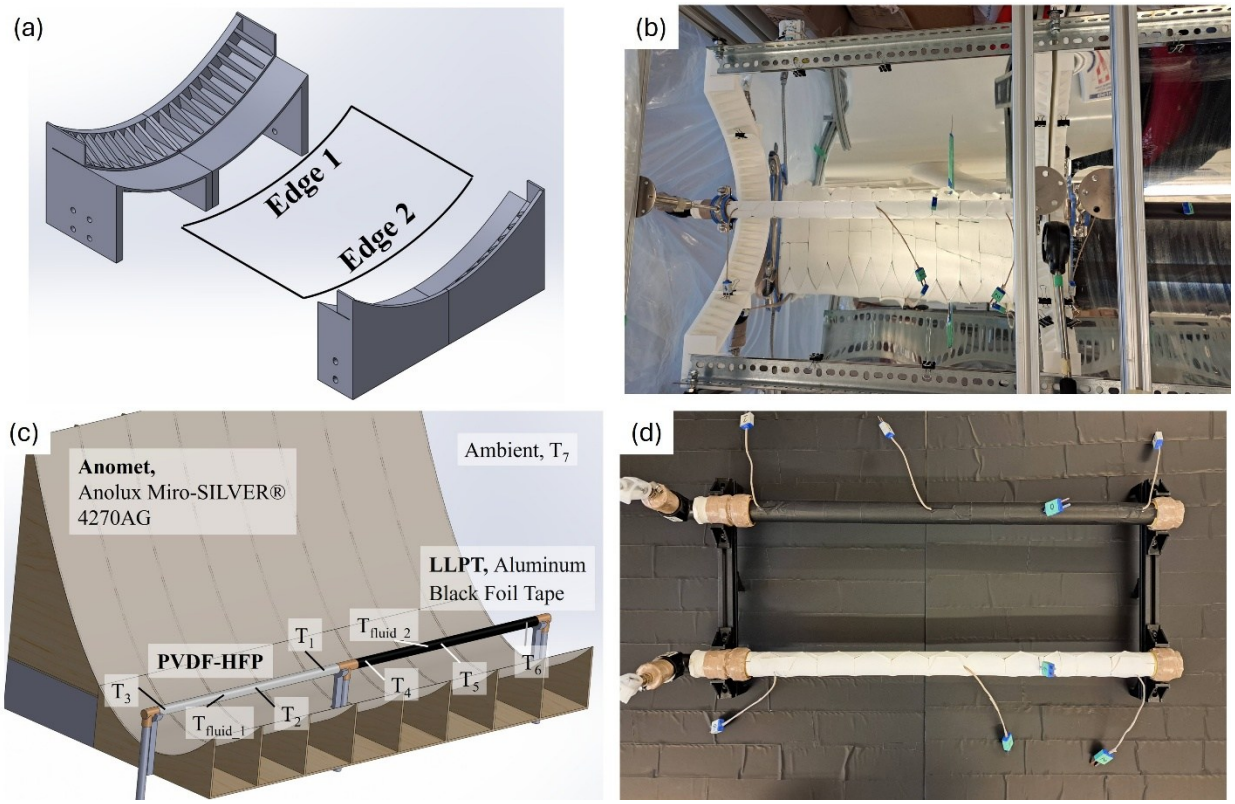

Figure 4-1: Experimental trough configuration setup: (a) 3D-printed channels used to constrain the reflective aluminum sheet into a parabolic geometry, (b) complete trough-enhanced structure with tubular RC and reference emitters, (c) thermocouple placement illustrated by a CAD model, and (d) reference configuration without the parabolic trough reflector.

4.2.3. Fabrication of Hierarchy Porous P(VdF-HFP) Membranes

The PVDF-HFP membranes were fabricated via a non-solvent-induced phase separation (NIPS) process. The weight ratio of the polymer (PVDF-HFP), solvent (acetone), and nonsolvent

(deionized water) was maintained at 1:8:1.25. This optimized composition, adapted from Pirvaram et al. [23], has been reported to yield enhanced UV-NIR reflectance and high mid-infrared (MIR) emittance.

Initially, acetone (56 g) was sealed in a 125 mL flask and heated to 40 °C. PVDF-HFP pellets (8 g) were then added and stirred at 1000 rpm for 30 minutes until a clear and homogeneous solution was obtained. Deionized water (8.75 mL) was subsequently added dropwise via a syringe over 2 minutes under continuous stirring, and the mixture was further stirred for an additional 30 minutes to promote controlled phase inversion.

The resulting solution (~80 mL) was allowed to cool for 30 minutes, with the room surroundings at 25 °C, and subsequently cast in varying volumes into two different sizes Petrie dishes. The container was covered with aluminum foil perforated with small holes to control solvent and nonsolvent evaporation. The film was then left undisturbed on a horizontal surface for 72 hours to dry and solidify. The resulting membrane was carefully detached and mounted onto a copper pipe using thermal adhesive tape (Gdrtwwh, Gdrtwwh Inc.) for subsequent experiments. The casting solution volumes corresponding to different Petrie dish sizes are summarized in Table 4-1. A comparative assessment of the three samples with respect to optical and thermal properties was conducted to determine the most suitable configuration. The identified optimal sample was then scaled up for mass production and employed in the outdoor experimental tests.

Table 4-1: Casting conditions: solution volumes and corresponding Petrie dish sizes used for membrane preparation.

Sample	Petrie dishes diameter (cm)	Casting solution volume (mL)
1 (9 cm, 25 mL)	9	25
2 (9 cm, 20 mL)	9	20
3 (10 cm, 25 mL)	10	25

4.2.4. Material Property Characterization

Four key properties of the hierarchically porous P(VdF-HFP) membranes were characterized owing to their critical influence on radiative cooling performance: solar reflectance, longwave infrared emittance, thermal conductivity, and membrane thickness.

The optical properties in the 0.3–2.5 μm wavelength range, which encompasses the ultraviolet (UV), visible (VIS), and near-infrared (NIR) regions and accounts for ~99 % of solar irradiance, were examined. The spectral range of 4–20 μm—which spans the mid-wave infrared (MWIR, 4–8 μm), long-wave infrared (LWIR, 8–15 μm), and part of the far-infrared (FIR, 15–20 μm), covers ~73.5% of the thermal emission from a blackbody at a temperature of 300 K. Spectral hemispheric transmittance and reflectance in the 0.3–1.1 μm wavelength range were measured using a UV-VIS-NIR spectrophotometer (Shimadzu UV-2600i Plus) equipped with an integrating sphere (ISR-2600Plus). Measurements in the 1.1–2.5 μm range were performed using a Fourier Transform Infrared (FTIR) spectrometer (Bruker Vertex 70) with an integrating sphere (Mid-IR IntegratIR™). In addition, spectral hemispheric transmittance and reflectance in mid-wave infrared (4–8 μm), long-wave infrared (8 –15 μm) and partial far-infrared (15–20 μm) regions were characterized using the same FTIR setup.

Based on Kirchhoff's law, the spectral absorptance (α) and emittance (ε) were calculated using the equation $\alpha_\lambda' = 1-\rho_\lambda'-\tau_\lambda'$, where ρ_λ' and τ_λ' denote the spectral directional reflectance and transmittance, respectively. The solar absorptance (over the spectral range from 0.3–2.5 μm) and infrared emittance (4–20 μm) were derived from the measured optical properties. The total hemisphere solar reflectance was obtained by integrating the product of the measured solar reflectance and the global title irradiance spectrum over 0.3–2.5 μm. Similarly, the total hemisphere emittance within atmospheric windows (8–13 μm) and infrared band (4–20 μm) were determined by integrating the product of the calculated spectral emittance and the 300 K blackbody radiation spectrum over corresponding ranges.

The thermal conductivity of the membrane was measured using the modified transient plane source (MTPS) method with a C-Therm TCI-3A analyzer. To minimize the dependency of the measurement results on the sample thickness the instrument was calibrated with the blotter testing method. The membrane thickness was determined by optical microscopy (ZEISS ApoTome.2). For sample preparation, the membrane was rapidly solidified in liquid nitrogen and fractured into small pieces to prevent deformation during cutting.

4.2.5. Temperature and Environmental Condition Measurement

Temperature measurements were acquired using an NI-9213 datalogger (National Instrument) coupled with an NI-9162 USB carrier. The built-in cold junction compensation was employed to mitigate the influence of ambient temperature fluctuations during outdoor testing. A total of nine T-type thermocouples were deployed to monitor the fluid temperature, coated surfaces and ambient

air.

A pyranometer (Renke, RS-TBQ-N01-AL) was employed to record the incident solar radiation. The measurement uncertainty of the pyranometer was evaluated following the Guide to the Expression of Uncertainty in Measurement (GUM) framework [59]. The reported uncertainty corresponds to a standard uncertainty multiplied by a coverage factor of $k_C = 2$, representing a confidence level of approximately 95%. The final expanded uncertainty was determined to be 17.1%. In addition, an anemometer (Bentech, GT8907) was utilized to monitor the wind flow speed.

4.2.6. Fluid Cooling Performance Calculations

The thermal circuit representing the heat transfer mechanisms involved in the structure comprising the cooper pipe coated with the PDRC material is illustrated in Figure 4-2.

The net cooling power applied to the fluid, $P_{cooling}$ can be determine by two approaches. The first approach, adopted in this experiment, is based on the measured fluid mean temperature difference (°C per hour, $\triangle T_{fluid}$) across the RC system (Equation (4-1)). The second approach, used for comparison, is to numerically estimate the radiative cooling power ($P_{cooling}$) as an integration of the sum of the RC net thermal radiative emission, incident solar power (P_{solar}) and ambient air convection (P_{conv}), as described in Equations (4-2).

$$P_{cooling} = -m \cdot C_P \cdot \triangle T_{fluid} \tag{4-1}$$

$$P_{cooling} = P_{rad}\left(P_{RC} - P_{atm} - P_{earth} - P_{space}\right) - P_{solar} - P_{conv}(T_{atm}, T_{RC}) \tag{4-2}$$

where P_{rad} denotes the net radiative power emitted from the RC surface to deep space as a function of RC thermal emission power (P_{RC}), incoming ambient air radiation (P_{atm}), incoming earth radiation (P_{earth}), incoming deep-space radiation (P_{space}), P_{solar} represents the absorbed solar irradiance on the RC surface, and P_{conv} corresponds to convective heat exchange between the RC surface and ambient air. Here, m is the fluid mass, C_P the specific heat capacity of the fluid, and $\triangle T_{fluid}$ the mean fluid temperature difference per second.

When $P_{cooling} > 0$, the RC system dissipates more heat in the form of thermal radiation to outer space than the amount of heat it absorbs from ambient air, the ground, and solar radiation. This process is experimentally reflected by a decrease in fluid temperature ($\triangle T_{fluid} < 0$). Conversely, when $P_{cooling} < 0$, the RC system experiences a net heat gain because the heat transferred from the surroundings exceeds the amount of heat radiated to outer space, resulting in an increase in fluid temperature ($\triangle T_{fluid} > 0$).

The detailed mathematical formulations for each heat transfer component are presented in Equations (2) to (4).

$$P_{rad} = \oiint dA\left(P_{RC} - P_{atm} - P_{earth} - P_{space}\right) \tag{4-3}$$

$$P_{solar} = \oiint dA\left(P_{direct} \cdot C_g + P_{diffuse}\right) \tag{4-4}$$

$$P_{conv} = \oiint dA \cdot h \cdot (T_{air} - T_{RC}) \tag{4-5}$$

where $\oiint dA$ represents the surface integration over the RC emitter and the convective heat transfer between the RC surface and the ambient air is denoted by ***h.***

The radiative heat exchange components (i.e., P_{RC}, P_{atm}, P_{earth} and P_{space}) were determined using the Monte Carlo Ray Tracing (MCRT) method, as described in Chapter 3. The total solar irradiance incident on the RC surface consists of direct (P_{direct}) and diffuse ($P_{diffuse}$) components. The correlation between direct and global solar irradiation was established by Orgill et. al [53]. Under clear and non-humid daytime conditions, the global solar irradiance can be approximated as 82.3% direct and 17.7% diffuse radiation.

The geometric solar concertation ratio, C_g, is defined as:

$$C_g = \frac{W_{trough}}{\left(D_{pipe} + 2 \cdot t_{RC} + 2 \cdot t_{tape}\right)} \tag{4-6}$$

where W_{trough} is the top opening width of the parabolic trough, D_{pipe} is the outer diameter of the copper pipe, t_{RC} is thickness of the RC membrane, and t_{tape} is the thickness of the thermal adhesive tape.

The total thermal resistance (R_t) of the tubular configuration consists of contributions from the RC membrane (R_{RC}), thermal tape (R_{tape}), copper pipe (R_{pipe}), and internal fluid (R_{fluid}), as described in Equations (7). The corresponding temperature nodes are illustrated in Figure 4-2.

$$R_t = R_{RC} + R_{tape} + R_{pipe} + R_{fluid} \tag{4-7}$$

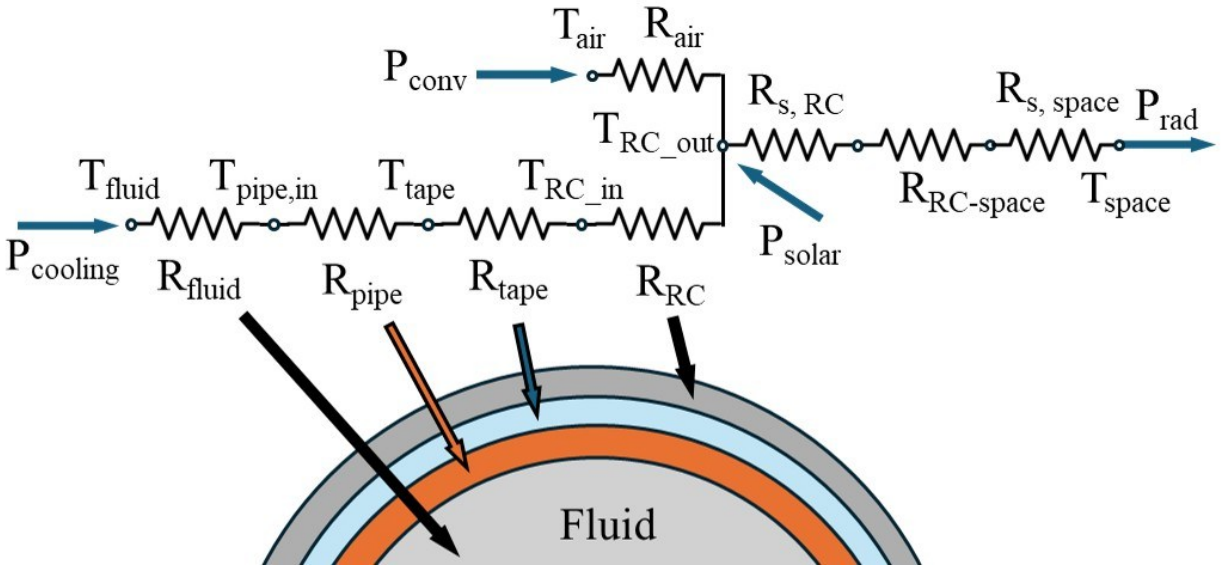

Figure 4-2: Schematic of the thermal circuit for the tubular configuration. T_{air} denotes the ambient air temperature, T_{space} denotes the temperature of outer space, $T_{pipe,\ in}$ denotes the interface temperature between the fluid and cooper pipe, T_{tape} denotes the interface temperature between the thermal tape and cooper pipe outer surface, $T_{RC,\ in}$ denotes the interface temperature between the thermal tape and RC membrane, and $T_{RC,\ out}$ represents the outer surface temperature of the RC membrane. $R_{s.RC}$ and $R_{s.space}$ are the surface resistance in radiative heat transfer, while $R_{RC\text{-}space}$ is the space resistance between RC and outer space.

4.3. Results

Section 4.1 presents the characterization results for PVDF-HFP membranes prepared with different casting solution volumes during the phase inversion process. Section 4.2 reports the dimensional uniformity and property deviation of the optimized casting volumes. Section 4.3 provides the outdoor testing outcomes and evaluates the practical cooling performance. Finally, Section 4.4 compares the numerical analysis with experimental results.

4.3.1. Characterization of Membranes Prepared with Different Casting Solution Volumes

Figure 4-3a to Figure 4-3i presents the thickness measured at the center and two sides of three PVDF-HFP membranes prepared with different casting solution volumes, along with the corresponding thermal conductivity of these samples (see Table 4-1). The results indicate that the minimum thickness across the sample generally appears near the membrane center, although some deviations are observed at other locations. Sample 1 (9 cm, 25 mL) exhibits a thermal conductivity of 0.052 $W \cdot m^{-1} \cdot K^{-1}$ and the lowest thickness deviation (48 μm). Sample 2 (9 cm, 20 mL) shows a thermal conductivity of 0.064 $W \cdot m^{-1} \cdot K^{-1}$ with a thickness deviation of 99 μm. Sample 3 (10 cm, 25 mL) has a thermal conductivity of 0.057 $W \cdot m^{-1} \cdot K^{-1}$ and the largest thickness deviation (123 μm).

The increased non-uniformity is attributed to shrinkage-induced deformation during solvent evaporation. Specifically, longitudinal and lateral shrinkage is attributed to smooth substrates, which reduce the membrane-surface bonding. Additionally, high viscoelasticity of PVDF-HFP promotes membrane lateral shrinkage during drying, while its intrinsically weak interfacial affinity with the surface of the glass substrate leads to pronounced edge contraction. This effect becomes more significant when the casting solution depth in the Petrie dish is low, which results in greater thickness increase near the membranes edge.

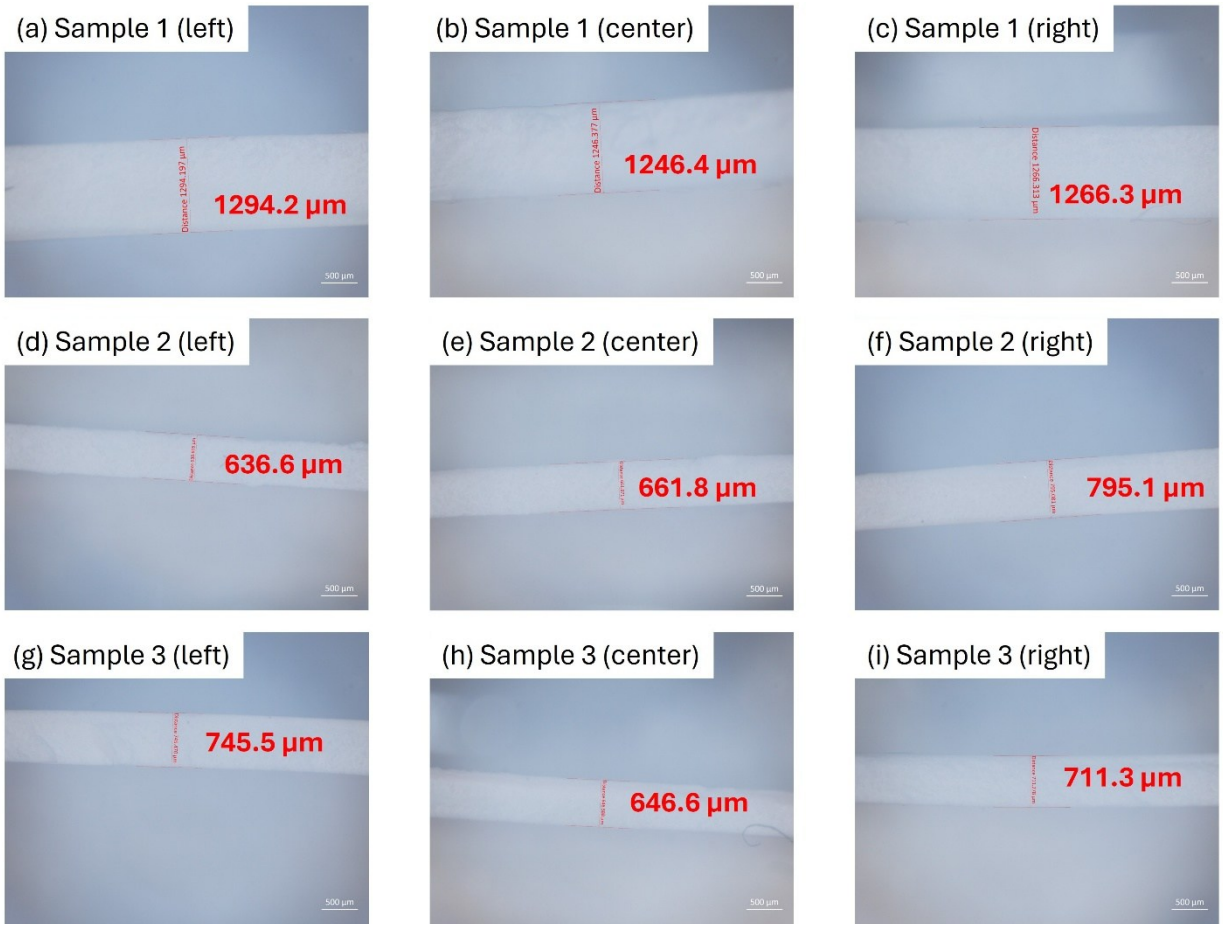

Figure 4-3: The thickness variation of the membrane sample 1–3.

(a-c) Sample 1 (9 cm, 25 mL): 1294.2 µm (left), 1246.4 µm (center), and 1266.3 µm (right); thermal conductivity: 0.052 $W \cdot m^{-1} \cdot K^{-1}$.

(d-f) Sample 2 (9 cm, 20 mL): 636.6 µm (left), 661.8 µm (center) and 795.1 µm (right) ; thermal conductivity: 0.064 $W \cdot m^{-1} \cdot K^{-1}$.

(g-i) Sample 3 (10 cm, 25 mL): 745.5 µm (left), 646.6 µm (center) and 711.3 µm (right); thermal conductivity: 0.057 $W \cdot m^{-1} \cdot K^{-1}$.

The spectral hemisphere solar reflectance and spectral hemisphere infrared emittance are presented in Figure 4-4 and Figure 4-5, respectively. The results in Figure 4-4 and Figure 4-5 depict the impact of the PVDF-HFP thickness on optical properties. The total solar reflectance of sample 1–3 was 0.982, 0.977 and 0.979, respectively. The deviation in total solar reflectance among the samples is less than 1 %, consistent with previous findings that the thickness of PVDF-HFP

membranes has a negligible influence on modifying the porous structure when it exceeds 850 μm, as reported by Pirvaram [60]. Moreover, such porous structures are sufficient to achieve a high solar reflectance of approximately 0.95 once the membrane thickness reaches 300 μm, as according to Mandal et al [27]. The total atmospheric emittance within 8 to 13 μm is 0.937, 0.937 and 0.941 for Samples 1–3, while the total infrared emittance within 4 to 20 μm is 0.885, 0.879 and 0.878, respectively. For comparison the reference blackbody emitter (LLPT black aluminum foil tape) exhibits emittance values of 0.918 and 0.937 over the 8-13 μm and 4-20 μm spectral ranges, respectively. The result shows that Sample 1 has the best total reflectance and total infrared emittance. Overall, Sample 1 demonstrates the lowest surface thickness deviation and the highest total solar reflectance and infrared emittance among the tested membranes. Consequently, the methods used to cast Sample 1 were used to prepare samples for subsequent experiments.

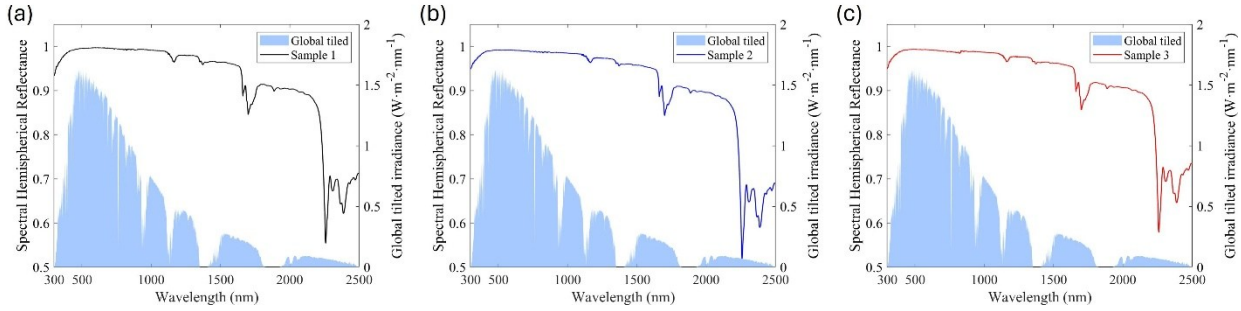

Figure 4-4: The spectral infrared emittance for (a) sample 1, (b) sample 2 and (c) sample 3.

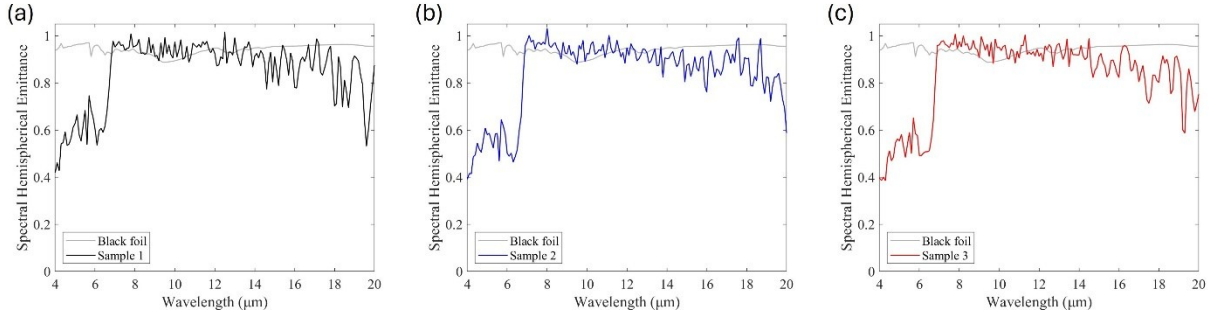

Figure 4-5: The spectral infrared emittance for (a) sample 1, (b) sample 2 and (c) sample 3. The light grey curve is the reference blackbody emitter emittance spectrum.

4.3.2. Dimensional Uniformity and Property Deviation of the Optimized Casting Volume

The property variations among laboratory-fabricated batches of 30 samples, all cast with 25 mL solution into Petrie dishes with a diameter of 9 cm, were assessed to determine reproductivity and scalability. Figure 4-6a shows the frequency distribution of membrane diameters, while Figure 4-6b and Figure 4-6c presents the spectral hemisphere reflectance within 0.3–2.5 μm and the spectral hemisphere infrared emittance within 4 to 20 μm. The median diameter was 6.2 cm, with the largest and smallest samples having a diameter that measured 7.0 cm and 5.4 cm, respectively. The summarized properties of the largest, median and smallest samples were presented in Table 4-2.

The results indicates that the solar reflectance ($\rho_{0.3\_2.5}$), atmospheric emittance (ε_{8_13}), and infrared emittance (ε_{4_20}) vary by only ~1.5 %, and the thermal conductivity (k) varies by ~4% between the thickest and thinnest samples when compared to the median-diameter (6.2 cm) sample. However, the thickness deviation shows a much larger variation. The thickness of the smallest RC sample, which had a diameter of 5.4 cm, was measured to be 1045.9 μm, 1443.3 μm and 1384.7 μm at its center, half-diameter and edge, respectively. The median sample (diameter of 6 cm) exhibited corresponding thickness values of 908.4 μm, 994.7 μm and 1224.7 μm. The largest sample (diameter of 7.4 cm) showed corresponding thicknesses of 731.3 μm, 740.4 μm and 884.3 μm. The observed dimensional deviation is attributed to additional acetone leaking during the solvent evaporation caused by a mismatch between the Petrie dish and aluminum sealing foil, which accelerates polymer precipitation and signifies local and edge contraction. To minimize thickness deviation, the largest (7 cm diameter) and smallest (5.4 cm diameter) samples were excluded from RC coating. In addition, the peripheral edge of each membrane was trimmed to ensure a more

uniform thickness across the active area. This approach ensured that the coated membranes used in subsequent experiments exhibited consistent structural and optical characteristics.

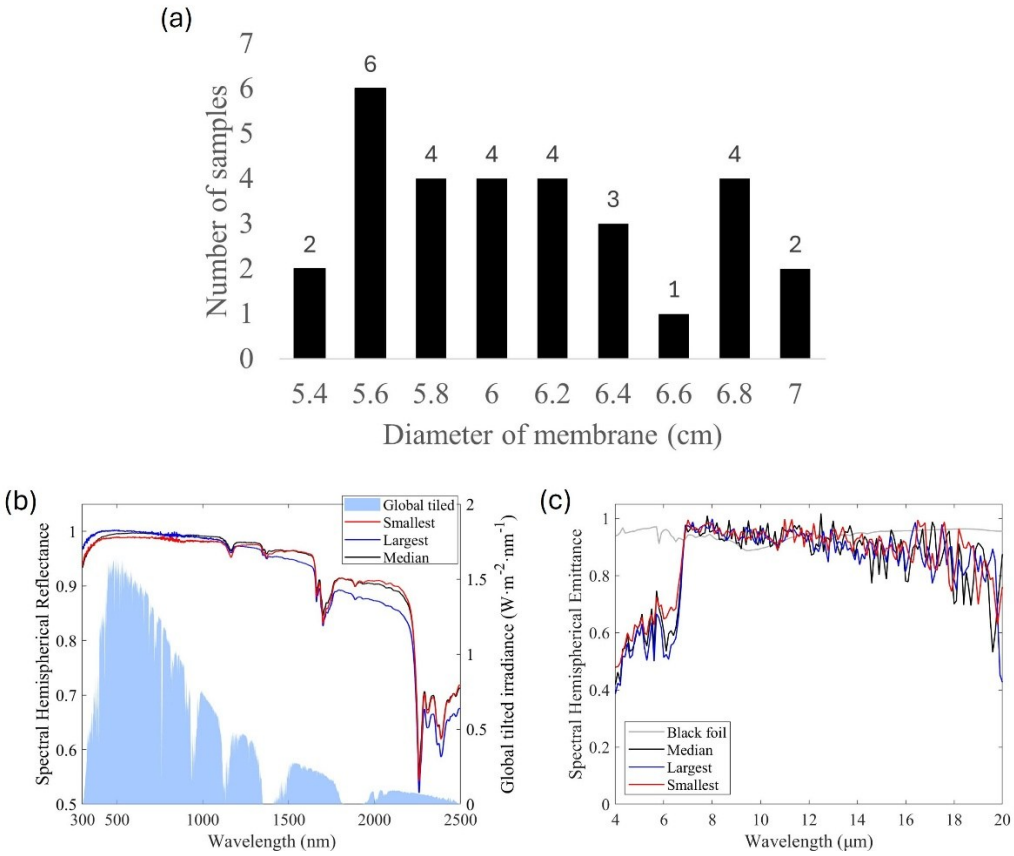

Figure 4-6. Dimensional and optical properties of the fabricated samples: (a) dimeter distribution, (b) spectral hemispherical reflectance in 0.3–2.5 μm range, and (c) spectral hemispherical infrared emittance in 4–20 μm range.

Table 4-2: The summarized properties of the largest, median and smallest samples.

Diameter (cm)	Center thickness (μm)	$\rho_{0.3\text{-}2.5}$	ε_{8-13}	ε_{4-20}	k ($W \cdot m^{-1} \cdot K^{-1}$)
5.4	1045.9	0.975	0.94	0.898	0.051
6	908.4	0.981	0.937	0.885	0.052
7	731.3	0.981	0.934	0.88	0.053

4.3.3. Outdoor Testing Results and Practical Cooling Performance

The cooling performance of the parabolic trough-enhanced radiative cooler was tested from 15:00 on September 18 to 15:00 on September 19, 2025, while the configuration without the trough was tested from 17:00 on September 16 to 17:00 on September 17, 2025. Both experiments were conducted on the rooftop of the Bergeron Centre for Engineering Excellence at the Keele campus of York University, Toronto. Appendix A presents an energy-balance calculation used to verify that the measured fluid-temperature changes are physically consistent with the predicted cooling power.

Figure 4-7 presents experimental results, including wind speed, incident solar radiation distribution (Figure 4-7a), sub-ambient cooling performance (Figure 4-7b), and temperature distribution of the RC emitter (Figure 4-7c) and reference blackbody emitter (Figure 4-7d) over a 24-h testing period. As shown in Figure 4-7b, the internal water temperature of the RC emitter pipe reached a maximum sub-ambient cooling of 4.1 °C at 14:27 and a minimum sub-ambient cooling of 1.2 °C at 12:15 during the daytime (10:00–15:00 on September 19). In contrast, the reference blackbody emitter exhibited significant negative sub-ambient cooling (i.e. its temperature was 4–9 °C above ambient) during the same period. At nighttime and early morning (18:00–06:00), both the RC emitter and the reference blackbody emitter exhibited sub-ambient cooling of 2–4 °C, in the absence of solar radiation. Notably, under fully cloudy conditions (15:00–16:00 on September 18 and 07:00–10:00 September 19; Figure 4-7a), the RC emitter still maintained a temperature of 2 °C less than the ambient temperature, demonstrating the effectiveness of radiative cooling under both clear and cloudy skies.

As shown in Figure 4-7c, the surface temperature of the RC emitter at one-quarter and one-half of the trough length remained consistently below the air temperature, whereas the edge regions

exhibited higher surface temperatures between 10:00 and 14:00. It is expected that localized heating at the edge region reduced the cooling power effect and this is attributed to the larger view factor the edge has with surrounding terrestrial objects (e.g., concreate titles and plastic coverings) compared with the trough reflector. As the surrounding objects absorbed solar radiation and warmed up, they emitted infrared radiation toward the edge region of the RC emitter, raising the temperature above ambient.

By comparison, the water in the pipe coated with a reference blackbody emitter, which absorbed the solar radiation directly, remained at least 5 °C above ambient between 10:00 to 15:00, although it still exhibited a ~2 °C sub-ambient cooling effect during the nighttime (18:00–06:00).

Notably, the reference blackbody emitter maintains a relatively unform temperature across its entire tubular surface, as the high thermal conductivity of aluminum (k = 237 W/m·k) allows rapid lateral heat redistribution. even though each section of the tubular emitter undergoes a different radiative heat transfer. In contrast, the porous PVDF-HFP membranes, low thermal conductivity (k = 0.052 W/m·k) restrict heat spreading, leading to local temperature differences.

At night (00:00), the water inside the RC emitter is 14.5 °C, while the RC membrane surface temperature ranged from 13.9 °C at the trough center to15.8 °C at the edge is. In comparison, the water inside the reference blackbody emitter was 15.3 °C, with a near uniform surface temperature between 15.0 and 15.8 °C. During daytime (12:00), the RC emitter surface temperature varied from 21.4 °C at the trough center to 25.6 °C at the edge, whereas the reference blackbody emitter exhibited significantly higher temperatures of 29.3 and 33.1 °C at the center and edge, respectively. These results further demonstrate the superior passive daytime radiative cooling capability and lower thermal conductivity effect of the PVDF-HFP-based RC emitter compared with the

aluminum-based reference emitter.

Plastic end caps were employed to reduce wind intrusion and suppress convective heat losses from the emitters, as shown in Figure 4-7e. However, their use introduces two adverse effects. First, the caps absorb solar radiation and attain a higher surface temperature than the surrounding environment, leading to additional long-wave radiative loading on the emitter. Second, by restricting air exchange between the trough interior and the ambient environment, the end caps increase the internal air temperature, thereby diminishing the net cooling potential. These effects indicate that material selection for end caps particularly solar absorptivity and infrared emissivity can meaningfully influence the thermal environment around the emitter.

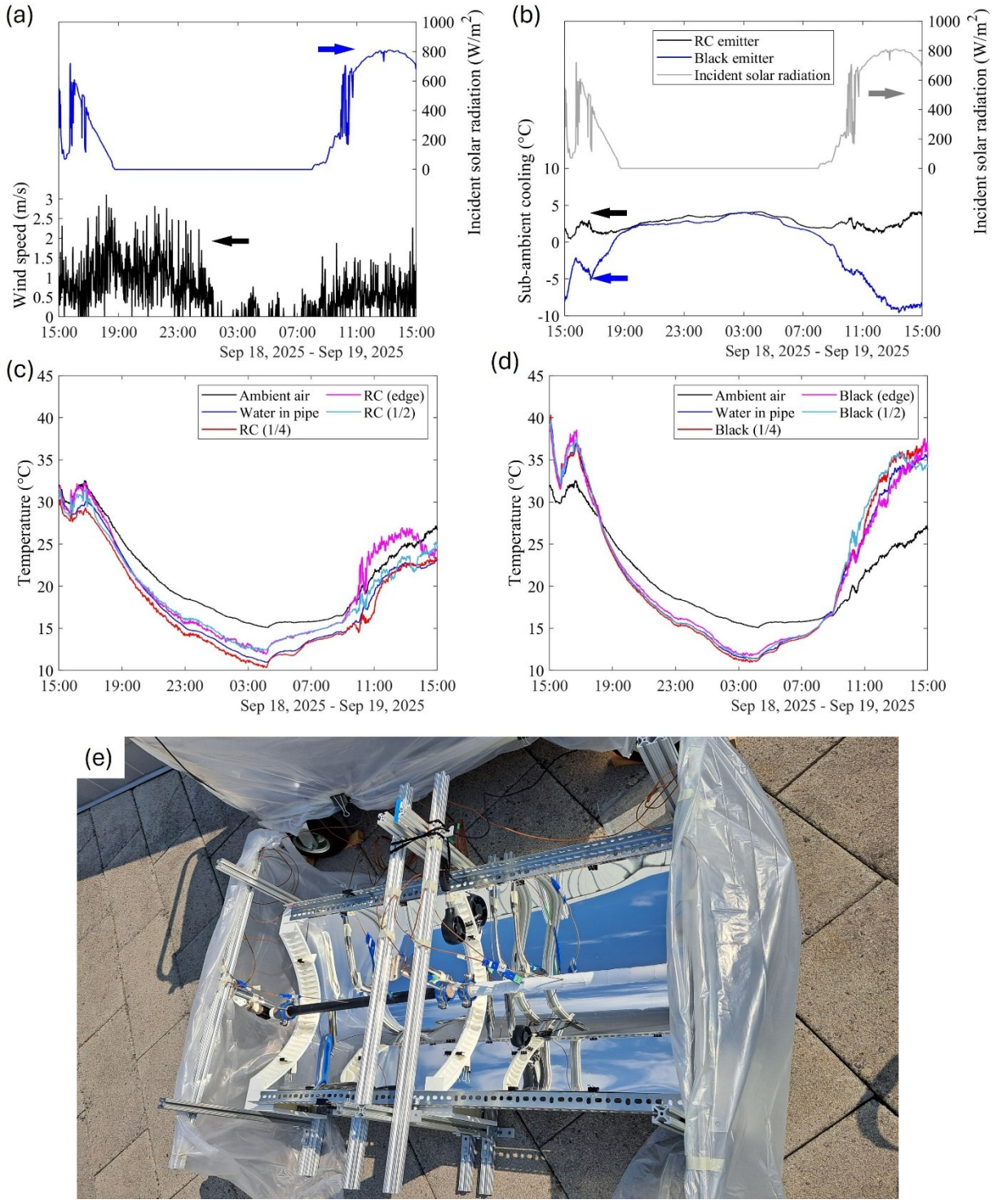

Figure 4-7. Measurement result for the trough-enhanced configuration: (a) solar irradiance and wind speed, (b) sub-ambient cooling effect, (c) temperature distribution of the RC emitter, (d) temperature distribution of the blackbody emitter, and (e) the edge influence from the surroundings.

The configuration without the trough was tested to isolate and evaluate the effect of the trough reflector, from 17:00 on September 16 to 17:00 on September 17, 2025. Figure 4-8 shows the results, including the wind speed and solar radiation distribution (Figure 4-8a), sub-ambient cooling performance (Figure 4-8b), temperature distribution of the RC emitter (Figure 4-8c), and that of the reference blackbody emitter (Figure 4-8d). As illustrated in Figure 4-8b, the RC emitter consistently exhibited a sub-ambient cooling effect during a 24-h test, whereas the reference blackbody emitter displayed a strong sensitivity to incident solar radiation.

As shown in Figure 4-8c and Figure 4-8d, the water inside the tubular RC emitter remained approximately 1.4 °C below the ambient temperature between 8:00 and 18:00, while the water in the reference blackbody emitter was ~6.0 °C above the ambient in the same period. At night (18:00–6:00), both systems demonstrated sub-ambient cooling, with the RC and the reference blackbody emitters reaching ~2.2 °C and ~2.1 °C below ambient, respectively.

It is noteworthy that the reference blackbody emitter exhibited a delayed thermal response to incident solar radiation. When the solar irradiance first became nonzero at 07:35, the water temperature inside reference blackbody emitters did not reach ambient until 9:24. This delay is attributed to the high specific heat capacity of water, which slows its thermal response. A similar phenomenon was observed for the water inside the RC emitter: as the ambient air was heated by solar radiation, the water maintained a relatively lower temperature, thereby producing a pronounced sub-ambient cooling effect during the same period.

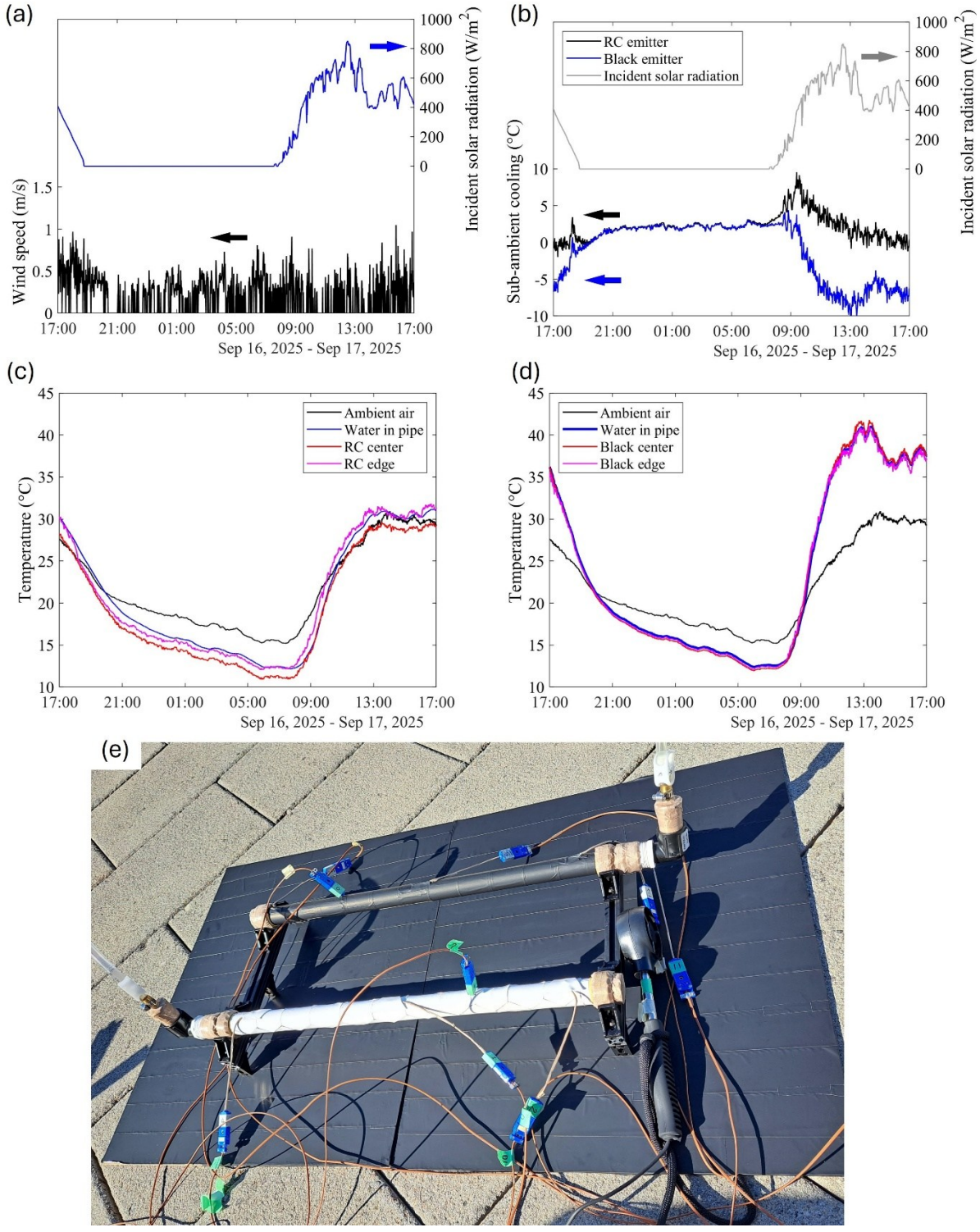

Figure 4-8: Measurement result for the configuration without the trough: (a) solar irradiance and wind speed, (b) sub-ambient cooling effect, (c) temperature distribution of the RC emitter, (d) temperature distribution of the blackbody emitter, and (e) configuration without the trough used as a reference comparison.

4.3.4. Validation of the numerical analysis results through outdoor testing results and practical cooling performance

The temperature profile and corresponding weather condition of the trough-enhanced configuration at 12:00 and 00:00 are selected to evaluate the numerical analysis results on daytime and nighttime radiative cooling performance. The experimental results are summarized in Table 4-3. Since the temperature of surrounding terrestrial objects (e.g., concreate tile and plastic cover) was unknown, it was assumed to be a grey cement roofing tile, with a thermal emittance of 0.94 [61] and 10 °C above ambient throughout the day. The convection heat transfer coefficient was estimated using Churchill-Bernstein correction with a 25% experimental uncertainty, while the incident solar radiation carried a 17.1 % measurement uncertainty.

Table 4-3: Experimental environmental condition and measured RC temperature of noontime and mid-night on September 19.

Time (Est)	Measured RC pipe water temperature (°C)	Measured blackbody pipe water temperature (°C)	Ambient temperature (°C)	Solar radiation (W/m^2)	Wind speed (m/s)
12:00	21.9	30.9	23.7	765	0.79
00:00	14.5	15.3	17.93	0	0.81

The numerical temperature predicted RC emitter temperature at 12:00 is presented in Figure 4-9a, as a function of incident solar radiation and ambient air convection coefficient. The experimental data shows approximately 1 °C higher temperature than the red-highlighted region predicted by the model. In contrast, the measured blackbody emitter temperature (30.9 °C) is significantly lower than the numerically estimated lowest value (34.2 °C). The deviation is attributed to the

uncertainties in the assumed convection coefficient, cloud coverage, surrounding surface temperature.

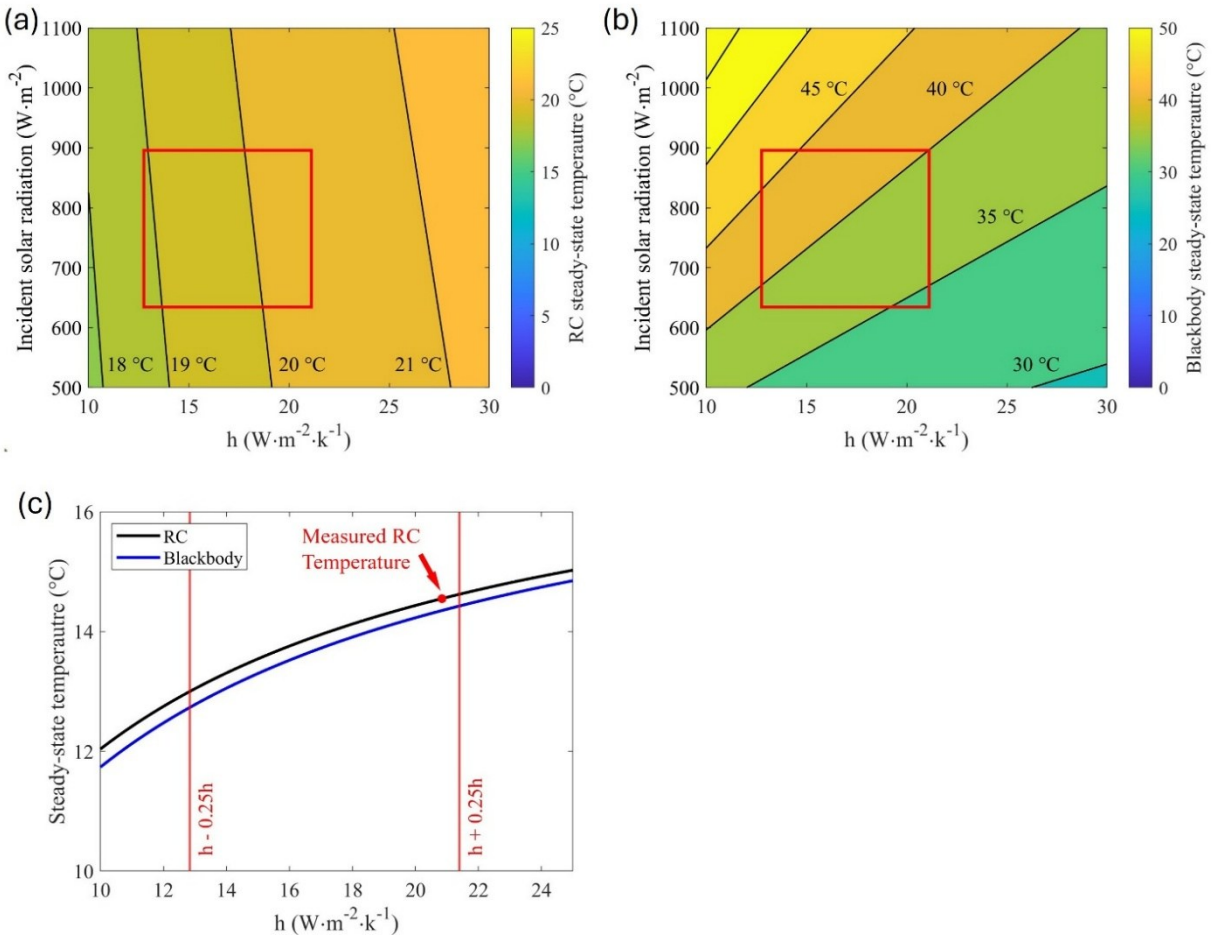

Figure 4-9: Numerical analysis on emitter temperature with parabolic trough at 12:00 for (a) RC emitter (b) blackbody emitter. (c) Numerical analysis on emitter temperature with parabolic trough at 10:00 for RC emitter. The red highlighted region indicates the combined uncertainty range, accounting for a 25% variation in the convection heat transfer coefficient and a 17.1 % measurement uncertainty in incident solar radiation.

Under nighttime condition (00:00), with zero solar radiation, the model predicts an RC temperature of 12.9–14.6 °C when accounting for 25 % convection uncertainty and identical terrestrial assumption (in Figure 4-9b). The experimentally measured temperature of 14.5 °C falls near the

upper bound of numerical prediction. In comparison, the blackbody emitter is estimated to be 12.7–14.4 °C, while the measured temperature is 15.3 °C, showing a deviation of approximately 1 °C.

Overall, the close agreement between experimental and numerical results demonstrates the numerical method reliability in estimating RC emitter performance. The deviation suggests that the model slightly underestimates the convective and environmental effects under actual outdoor conditions. Further refinements are needed to reduce uncertainties, including the precise temperature of surrounding objects, humidity effects, and cloud coverage.

4.4. Conclusion

This study demonstrates that non-uniform solvent evaporation induces the dimensional variations in the fabricated PVDF-HPF membrane, resulting in a thinner thickness near the membrane center and a thicker region toward the edges. In addition, imperfect sealing between the aluminum foil and the Petrie dishes accelerates acetone evaporating, causing further shrinkage during the controlled solvent evaporation process. Despite these dimensional deviations, PVDF-HFP membranes exhibit negligible variations in their optical properties, maintaining high solar reflectance and strong thermal emittance within the atmospheric transparency window. These findings confirm that PVDF-HFP is a promising material for radiative cooling applications.

Outdoor testing depicted that the reference configuration without troughs provided sub-ambient cooling of ~1.2 °C during daytime and ~2.1 °C at night. With the addition of a parabolic trough reflector, the system maintains comparable baseline cooling performance while achieving peak sub-ambient cooling up to 4.2 °C during the day and 4 °C at night. Moreover, the RC emitter

demonstrated robust operation even under daytime cloud coverage, underscoring its potential for scalable development in practical cooling scenarios.

The numerical analysis results were in close agreement with experimental measurement, validating the reliability of the proposed model in predicting radiative cooling performance under appropriate assumptions on surrounding surface temperatures and experimental uncertainties are applied. This validation establishes confidence in employing the model as a predictive tool for system design and optimization. Nevertheless, further accuracy can be achieved by incorporating more precise data for the temperature of surrounding objects, as well as accounting for humidity and cloud cover effects.

Overall, the combined experimental and numerical findings highlight the effectiveness of PVDF-HFP-based radiative cooling systems and demonstrate the feasibility of enhancing their performance through optical concentrator designs such as parabolic trough reflectors. This work provides a foundation for advancing radiative cooling technologies toward practical applications in sustainable thermal management.

Chapter 5–Conclusion and Future Work

5.1. Summary of Research

This thesis explored the enhancement of radiative cooling (RC) performance through the integration of parabolic trough reflectors and the development of polymer-based RC emitters. The research was divided into three main objectives: (i) to numerically analyze the effect of trough geometry on the net radiative cooling power, (ii) to fabricate and optimize PVDF-HFP-based film RC emitters and systematically characterize their optical and thermal properties, and (iii) to experimentally validate the trough-enhanced RC performance using fabricated PVDF-HFP emitters under outdoor conditions.

Three-dimensional Monte Carlo ray tracing (MCRT) simulations were performed to investigate how the parabolic trough geometry, emittance spectrum, and solar angle influence system performance. The analysis revealed that trough integration enhances cooling by increasing the effective radiating area, blocking high-angle radiation from the atmosphere, and shading the emitter from direct solar gains.

In the experimental study, hierarchically porous PVDF-HFP membranes were fabricated using a controlled solvent evaporation process and integrated with aluminum troughs for outdoor

performance evaluation. Despite minor geometric deformation during fabrication, the optical properties remained stable, showing high solar reflectance and strong mid-infrared emittance. The experimental results confirmed that the trough-integrated RC system achieved significantly lower surface temperatures than the reference flat configuration under both daytime and nighttime conditions. The measured cooling behavior aligned well with the numerical predictions, with minor deviations attributable to unmodeled factors such as atmospheric humidity and reflections from surrounding objects. These findings demonstrate that trough-assisted radiative cooling effectively achieves sub-ambient temperature regulation for stationary water systems and holds potential for future extension to flowing-fluid applications.

5.2. Key Findings

1. Integration of parabolic trough reflectors enhances cooling performance by up to 2.53-fold (broadband emitter) and 2.45-fold (selective emitter) compared with a flat mono-facial RC under ideal reflective conditions. It is worth noting that for configurations previously reported in the literature only a two-fold enhancement was predicted.

2. Trough geometry scaling based on focal length remains valid for planar emitters, while tubular emitters show minor deviations, highlighting the importance of geometry–radiation coupling.

3. Outdoor experiments confirmed sub-ambient cooling of 1.2–4.2 °C below ambient during daytime and 2–4 °C at night, validating the theoretical predictions for stationary water system.

4. Numerical and experimental results exhibited strong agreement within the simplified boundary conditions, confirming the reliability of the MCRT-based model for predicting radiative cooling behavior under clear-sky, steady-state environments.

5. PVDF-HFP membranes maintained consistent optical performance despite fabrication-induced thickness variations, confirming their suitability for scalable RC fabrication.

5.3. Research Contributions

This work makes several key contributions to the field of passive radiative cooling and optical–thermal system design:

- A coupled numerical–experimental framework to evaluate trough-enhanced RC systems, bridging theoretical analysis with outdoor performance validation, was established.
- Insights into geometric scalability, showing how trough focal length, length and height affect the optical concentration and effective radiating solid angle were provided.
- The feasibility of PVDF-HFP membranes as durable, high-performance emitters for RC applications was demonstrated.
- The MCRT method was validated as a predictive design tool for optimizing trough-integrated RC configurations, offering a pathway toward adaptive, location-specific system designs.
- An integrated trough–tube RC concept was pioneered. This configuration is capable of cooling both stagnant and flowing media, laying the groundwork for future hybrid or large-scale implementations.

5.4. Limitations

While the results are promising, several limitations remain.

- The outdoor measurements were influenced by fluctuating weather conditions, including variable solar intensity, wind speed, and humidity.
- The fluid system application was limited to stationary water due to the combined constraints of system scalability, the high specific heat capacity of water, and the lack of an ultra-low-flow-rate pump. As a result, dynamic cooling behavior could not be experimentally characterized, and the analysis was restricted to no-flow conditions.
- The numerical model assumed steady-state boundary conditions and did not explicitly account for transient atmospheric variations such as cloud movement, sky temperature dynamics, and air humidity. In addition, the surrounding environment was simplified as a uniform horizontal surface, whereas in reality, the nearby structures are three-dimensional objects with their own optical and thermal properties, which can influence the effective view factor and the reflected longwave radiation incident on the radiative cooler.
- Minor fabrication imperfections in the PVDF-HFP membranes, caused by uneven solvent evaporation and sealing issues, introduced small uncertainties in surface morphology.

5.5. Future Work

Building on these findings, the following directions are recommended for future research:

- **System optimization:** Explore new trough geometries and reflective coatings with wavelength- and angle-selective properties to further improve daytime cooling.

- **Heat dissipation enhancement through thermal filler materials:** Previous studies have shown that hexagonal boron nitride (h-BN) exhibits optical properties comparable to PVDF-HFP while possessing much higher thermal conductivity. Developing a composite RC emitter combining PVDF-HFP and h-BN may improve in-plane heat spreading and enhance the overall radiative heat exchange efficiency.

- **Transient modeling:** Extend the MCRT–CFD coupling framework to incorporate time-dependent environmental factors and flow–radiation coupling for more accurate real-world predictions. Future models should also consider air humidity effects and three-dimensional surroundings with distinct optical properties to more accurately represent realistic outdoor boundary conditions.

- **Fluid dynamics coupling:** Extend the experimental system to include controlled low-flow liquid or gas circulation, enabling evaluation of the combined effects of convection and radiation on cooling power.

- **Active thermal compensation measurement:** Implement electrical heating control to maintain the fluid temperature equal to the ambient air temperature, allowing the electrical power to directly represent the net radiative cooling power. This approach

eliminates uncertainties associated with estimating convective heat transfer coefficients, particularly for stationary fluids, thereby improving the accuracy of cooling power quantification.

- **Hybrid integration:** Combine the trough-based RC system with solar thermal or heat pipe modules to enable continuous day–night operation.

- **Scaling and durability studies:** Conduct long-term outdoor tests to evaluate material stability, fouling resistance, and cooling efficiency under various climates.

- **Practical applications:** Assess the potential of trough-integrated RC for building rooftop cooling, fluid chiller systems, and off-grid thermal management.

5.6. Closing Remark

Overall, this thesis demonstrated that the combination of parabolic trough optics and radiative cooling emitters offers an effective and scalable pathway toward passive thermal regulation. The validated numerical model and experimental verification collectively underscore the feasibility of energy-free cooling systems capable of sub-ambient temperature control for fluid and surface applications. These findings contribute to the broader goal of developing sustainable, maintenance-free cooling technologies that can complement conventional energy systems in the transition toward a low-carbon future.

Reference

[1] N. Leob, “Tracking Changes in Earth’s Energy Budget”.
[2] B. Zhao, M. Hu, X. Ao, N. Chen, and G. Pei, “Radiative cooling: A review of fundamentals, materials, applications, and prospects,” *Appl. Energy*, vol. 236, pp. 489–513, Feb. 2019, doi: 10.1016/j.apenergy.2018.12.018.
[3] F. TROMBE, “PERSPECTIVES SUR L’UTILISATION DES RAYONNEMENTS SOLAIRES ET TERRESTRES DANS CERTAINES REGIONS DU MONDE,” *Perspect. SUR Util. Rayonnem. Sol. Terr. DANS Certain. Reg. MONDE*, 1975.
[4] J. P. Bijarniya, J. Sarkar, and P. Maiti, “Review on passive daytime radiative cooling: Fundamentals, recent researches, challenges and opportunities,” *Renew. Sustain. Energy Rev.*, vol. 133, p. 110263, Nov. 2020, doi: 10.1016/j.rser.2020.110263.
[5] X. Sun, Y. Sun, Z. Zhou, M. A. Alam, and P. Bermel, “Radiative sky cooling: fundamental physics, materials, structures, and applications,” *Nanophotonics*, vol. 6, no. 5, pp. 997–1015, Sept. 2017, doi: 10.1515/nanoph-2017-0020.
[6] B. Bartoli, S. Catalanotti, B. Coluzzi, V. Cuomo, V. Silvestrini, and G. Troise, “Nocturnal and diurnal performances of selective radiators,” *Appl. Energy*, vol. 3, no. 4, pp. 267–286, Oct. 1977, doi: 10.1016/0306-2619(77)90015-0.
[7] Y. Zhai *et al.*, “Scalable-manufactured randomized glass-polymer hybrid metamaterial for daytime radiative cooling,” *Science*, vol. 355, no. 6329, pp. 1062–1066, Mar. 2017, doi: 10.1126/science.aai7899.
[8] B. Orel, M. K. Gunde, and A. Krainer, “Radiative cooling efficiency of white pigmented paints,” *Sol. Energy*, vol. 50, no. 6, pp. 477–482, June 1993, doi: 10.1016/0038-092X(93)90108-Z.
[9] T. M. J. Nilsson and G. A. Niklasson, “Radiative cooling during the day: simulations and experiments on pigmented polyethylene cover foils,” *Sol. Energy Mater. Sol. Cells*, vol. 37, no. 1, pp. 93–118, Apr. 1995, doi: 10.1016/0927-0248(94)00200-2.
[10] C. G. Granqvist and A. Hjortsberg, “Surfaces for radiative cooling: Silicon monoxide films on aluminum,” *Appl. Phys. Lett.*, vol. 36, no. 2, pp. 139–141, Jan. 1980, doi: 10.1063/1.91406.
[11] C. G. Granqvist, A. Hjortsberg, and T. S. Eriksson, “Radiative cooling to low temperatures with selectivity IR-emitting surfaces,” *Thin Solid Films*, vol. 90, no. 2, pp. 187–190, Apr. 1982, doi: 10.1016/0040-6090(82)90648-4.
[12] T. M. J. Nilsson, G. A. Niklasson, and C. G. Granqvist, “A solar reflecting material for radiative cooling applications: ZnS pigmented polyethylene,” *Sol. Energy Mater. Sol. Cells*,

vol. 28, no. 2, pp. 175–193, Nov. 1992, doi: 10.1016/0927-0248(92)90010-M.
[13] J. Mandal, Y. Yang, N. Yu, and A. P. Raman, “Paints as a Scalable and Effective Radiative Cooling Technology for Buildings,” *Joule*, vol. 4, no. 7, pp. 1350–1356, July 2020, doi: 10.1016/j.joule.2020.04.010.
[14] E. Rephaeli, A. Raman, and S. Fan, “Ultrabroadband Photonic Structures To Achieve High-Performance Daytime Radiative Cooling,” *Nano Lett.*, vol. 13, no. 4, pp. 1457–1461, Apr. 2013, doi: 10.1021/nl4004283.
[15] “A Metamaterial Emitter for Highly Efficient Radiative Cooling - Hossain - 2015 - Advanced Optical Materials - Wiley Online Library.” Accessed: May 28, 2025. [Online]. Available: https://advanced.onlinelibrary.wiley.com/doi/10.1002/adom.201500119
[16] M. A. Kecebas, M. P. Menguc, A. Kosar, and K. Sendur, “Passive radiative cooling design with broadband optical thin-film filters,” *J. Quant. Spectrosc. Radiat. Transf.*, vol. 198, pp. 179–186, Sept. 2017, doi: 10.1016/j.jqsrt.2017.03.046.
[17] A. P. Raman, M. A. Anoma, L. Zhu, E. Rephaeli, and S. Fan, “Passive radiative cooling below ambient air temperature under direct sunlight,” *Nature*, vol. 515, no. 7528, pp. 540–544, Nov. 2014, doi: 10.1038/nature13883.
[18] Y. Xu, V. Ramanathan, and D. G. Victor, “Global warming will happen faster than we think,” *Nature*, vol. 564, no. 7734, pp. 30–32, Dec. 2018, doi: 10.1038/d41586-018-07586-5.
[19] D. Chae *et al.*, “Spectrally Selective Inorganic-Based Multilayer Emitter for Daytime Radiative Cooling,” *ACS Appl. Mater. Interfaces*, vol. 12, no. 7, pp. 8073–8081, Feb. 2020, doi: 10.1021/acsami.9b16742.
[20] Md. M. Hossain and M. Gu, “Radiative Cooling: Principles, Progress, and Potentials,” *Adv. Sci.*, vol. 3, no. 7, p. 1500360, 2016, doi: 10.1002/advs.201500360.
[21] N. Cheng *et al.*, “Nanosphere-structured hierarchically porous PVDF-HFP fabric for passive daytime radiative cooling *via* one-step water vapor-induced phase separation,” *Chem. Eng. J.*, vol. 460, p. 141581, Mar. 2023, doi: 10.1016/j.cej.2023.141581.
[22] A. Pirvaram, N. Talebzadeh, S. N. Leung, and P. G. O’Brien, “Radiative cooling for buildings: A review of techno-enviro-economics and life-cycle assessment methods,” *Renew. Sustain. Energy Rev.*, vol. 162, p. 112415, July 2022, doi: 10.1016/j.rser.2022.112415.
[23] A. Pirvaram, P. G. O’Brien, and S. N. Leung, “Fabrication and Optimization of Highly Solar Reflective and Long-Wavelength Infrared (LWIR) Emissive Porous Polymers for Passive Daytime Radiative Cooling,” in *Advanced Photonics Congress 2024 (2024), paper JM3D.3*, Optica Publishing Group, July 2024, p. JM3D.3. doi: 10.1364/BGPP.2024.JM3D.3.
[24] A. Pirvaram, S. N. Leung, and P. G. O’Brien, “The Global Warming Potential of Geoengineering via Radiative Cooling,” *Adv. Sustain. Syst.*, vol. 9, no. 5, p. 2400948, 2025,

doi: 10.1002/adsu.202400948.
[25] H. Ma *et al.*, "Multilayered SiO2/Si3N4 photonic emitter to achieve high-performance all-day radiative cooling," *Sol. Energy Mater. Sol. Cells*, vol. 212, p. 110584, Aug. 2020, doi: 10.1016/j.solmat.2020.110584.
[26] J. Mandal, "Hierarchically porous polymer coatings for highly efficient passive daytime radiative cooling." Accessed: June 13, 2025. [Online]. Available: https://www.science.org/doi/10.1126/science.aat9513
[27] K. Zhou, N. Miljkovic, and L. Cai, "Performance analysis on system-level integration and operation of daytime radiative cooling technology for air-conditioning in buildings," *Energy Build.*, vol. 235, p. 110749, Mar. 2021, doi: 10.1016/j.enbuild.2021.110749.
[28] E. Hosseinzadeh and H. and Taherian, "An Experimental and Analytical Study of a Radiative Cooling System with Unglazed Flat Plate Collectors," *Int. J. Green Energy*, vol. 9, no. 8, pp. 766–779, Nov. 2012, doi: 10.1080/15435075.2011.641189.
[29] Y. Lu *et al.*, "A Universal Route to Realize Radiative Cooling and Light Management in Photovoltaic Modules," *Sol. RRL*, vol. 1, no. 10, p. 1700084, 2017, doi: 10.1002/solr.201700084.
[30] J. N. Munday and T. Safi, "Radiative cooling of a GaAs solar cell to improve power conversion efficiency," in *2016 IEEE 43rd Photovoltaic Specialists Conference (PVSC)*, June 2016, pp. 1125–1127. doi: 10.1109/PVSC.2016.7749788.
[31] X. Sun, T. J. Silverman, Z. Zhou, M. R. Khan, P. Bermel, and M. A. Alam, "Optics-Based Approach to Thermal Management of Photovoltaics: Selective-Spectral and Radiative Cooling," *IEEE J. Photovolt.*, vol. 7, no. 2, pp. 566–574, Mar. 2017, doi: 10.1109/JPHOTOV.2016.2646062.
[32] M. Hu, G. Pei, Q. Wang, J. Li, Y. Wang, and J. Ji, "Field test and preliminary analysis of a combined diurnal solar heating and nocturnal radiative cooling system," *Appl. Energy*, vol. 179, pp. 899–908, Oct. 2016, doi: 10.1016/j.apenergy.2016.07.066.
[33] B. Zhao, M. Hu, X. Ao, and G. Pei, "Conceptual development of a building-integrated photovoltaic–radiative cooling system and preliminary performance analysis in Eastern China," *Appl. Energy*, vol. 205, pp. 626–634, Nov. 2017, doi: 10.1016/j.apenergy.2017.08.011.
[34] M. Hu, B. Zhao, J. Li, Y. Wang, and G. Pei, "Preliminary thermal analysis of a combined photovoltaic–photothermic–nocturnal radiative cooling system," *Energy*, vol. 137, pp. 419–430, Oct. 2017, doi: 10.1016/j.energy.2017.03.075.
[35] H. Fang *et al.*, "Performance evaluation of a metamaterial-based new cool roof using improved Roof Thermal Transfer Value model," *Appl. Energy*, vol. 248, pp. 589–599, Aug. 2019, doi: 10.1016/j.apenergy.2019.04.116.

[36] A. Castaldo, G. Vitiello, E. Gambale, M. Lanchi, M. Ferrara, and M. Zinzi, “Mirroring Solar Radiation Emitting Heat Toward the Universe: Design, Production, and Preliminary Testing of a Metamaterial Based Daytime Passive Radiative Cooler,” *Energies*, vol. 13, no. 16, Art. no. 16, Jan. 2020, doi: 10.3390/en13164192.
[37] J. Chen, L. Lu, Q. Gong, W. Y. Lau, and K. H. Cheung, “Techno-economic and environmental performance assessment of radiative sky cooling-based super-cool roof applications in China,” *Energy Convers. Manag.*, vol. 245, p. 114621, Oct. 2021, doi: 10.1016/j.enconman.2021.114621.
[38] J. Liu, Z. Zhou, J. Zhang, W. Feng, and J. Zuo, “Advances and challenges in commercializing radiative cooling,” *Mater. Today Phys.*, vol. 11, p. 100161, Dec. 2019, doi: 10.1016/j.mtphys.2019.100161.
[39] J. Peoples *et al.*, “Concentrated radiative cooling,” *Appl. Energy*, vol. 310, p. 118368, Mar. 2022, doi: 10.1016/j.apenergy.2021.118368.
[40] L. Zhou *et al.*, “Hybrid concentrated radiative cooling and solar heating in a single system,” *Cell Rep. Phys. Sci.*, vol. 2, no. 2, Feb. 2021, doi: 10.1016/j.xcrp.2021.100338.
[41] J. R. Hull and W. W. Schertz, “Evacuated-tube directional-radiating cooling system,” *Sol. Energy*, vol. 35, no. 5, pp. 429–434, Jan. 1985, doi: 10.1016/0038-092X(85)90132-X.
[42] M. Martin and P. Berdahl, “Summary of results from the spectral and angular sky radiation measurement program,” *Sol. Energy*, vol. 33, no. 3, pp. 241–252, Jan. 1984, doi: 10.1016/0038-092X(84)90155-5.
[43] S. B. Idso, “An experimental determination of the radiative properties and climatic consequences of atmospheric dust under nonduststorm conditions,” *Atmospheric Environ. 1967*, vol. 15, no. 7, pp. 1251–1259, Jan. 1981, doi: 10.1016/0004-6981(81)90316-4.
[44] Y. Dan, M. Hu, Q. Wang, Y. Su, and S. Riffat, “Comprehensive evaluation of integrating radiative sky cooling with compound parabolic concentrator for cooling flux amplifying,” *Energy*, vol. 312, p. 133673, Dec. 2024, doi: 10.1016/j.energy.2024.133673.
[45] E. du M. van Voorthuysen and R. Roes, “Blue Sky Cooling for Parabolic Trough Plants,” *Energy Procedia*, vol. 49, pp. 71–79, Jan. 2014, doi: 10.1016/j.egypro.2014.03.008.
[46] M. Sheng, H. Pan, D. Xu, and D. Zhao, “Characterization and performance enhancement of radiative cooling on circular surfaces,” *Renew. Sustain. Energy Rev.*, vol. 188, p. 113782, Dec. 2023, doi: 10.1016/j.rser.2023.113782.
[47] H. Zhang, “Preliminary analysis of a parabolic trough concentrating solar power system integrated with radiative cooling | International Journal of Low-Carbon Technologies | Oxford Academic.” Accessed: May 28, 2025. [Online]. Available: https://academic.oup.com/ijlct/article/doi/10.1093/ijlct/ctae050/7656744

[48] A. Pirvaram, T. Cooper, S. N. Leung, and P. G. O'Brien, "A comprehensive study on using underside infrared reflectors to enhance the performance of radiative cooling structures," *Energy Convers. Manag.*, vol. 304, p. 118180, Mar. 2024, doi: 10.1016/j.enconman.2024.118180.
[49] C. G. Granqvist and A. Hjortsberg, "Radiative cooling to low temperatures: General considerations and application to selectively emitting SiO films," *J. Appl. Phys.*, vol. 52, no. 6, pp. 4205–4220, June 1981, doi: 10.1063/1.329270.
[50] R. M. Goody, "A statistical model for water-vapour absorption," *Q. J. R. Meteorol. Soc.*, vol. 78, no. 336, pp. 165–169, Apr. 1952, doi: 10.1002/qj.49707833604.
[51] H. E. Bennett, J. M. Bennett, and M. R. Nagel, "Distribution of Infrared Radiance over a Clear Sky," *JOSA Vol 50 Issue 2 Pp 100-106*, Feb. 1960, doi: 10.1364/JOSA.50.000100.
[52] S. D. Lord, *A New Software Tool for Computing Earth's Atmospheric Transmission of Near- and Far-infrared Radiation*. Ames Research Center, 1992.
[53] J. F. Orgill and K. G. T. Hollands, "Correlation equation for hourly diffuse radiation on a horizontal surface," *Sol. Energy*, vol. 19, no. 4, pp. 357–359, Jan. 1977, doi: 10.1016/0038-092X(77)90006-8.
[54] E. and C. C. Canada, "Beaufort wind scale table." Accessed: Dec. 11, 2025. [Online]. Available: https://www.canada.ca/en/environment-climate-change/services/general-marine-weather-information/understanding-forecasts/beaufort-wind-scale-table.html
[55] "Phase Inversion Membranes & Immersion Precipitation." Accessed: Oct. 08, 2025. [Online]. Available: https://synderfiltration.com/learning-center/articles/introduction-to-membranes/phase-inversion-membranes-immersion-precipitation/
[56] K. Kimmerle and H. Strathmann, "Analysis of the structure-determining process of phase inversion membranes," *Desalination*, vol. 79, no. 2–3, pp. 283–302, Dec. 1990, doi: 10.1016/0011-9164(90)85012-Y.
[57] Ye. Bormashenko, R. Pogreb, O. Stanevsky, and Ed. Bormashenko, "Vibrational spectrum of PVDF and its interpretation," *Polym. Test.*, vol. 23, no. 7, pp. 791–796, Oct. 2004, doi: 10.1016/j.polymertesting.2004.04.001.
[58] L. N. Sim, S. R. Majid, and A. K. Arof, "FTIR studies of PEMA/PVdF-HFP blend polymer electrolyte system incorporated with LiCF3SO3 salt," *Vib. Spectrosc.*, vol. 58, pp. 57–66, Jan. 2012, doi: 10.1016/j.vibspec.2011.11.005.
[59] S. A. Bell, "A beginner's guide to uncertainty of measurement." Accessed: Oct. 18, 2025. [Online]. Available: https://eprintspublications.npl.co.uk/1568/
[60] A. Pirvaram, "Micro and Nano-structured Materials with Controlled Radiative Properties for Radiative Cooling Applications," Dec. 2024, Accessed: Oct. 09, 2025. [Online]. Available: https://hdl.handle.net/10315/42826

[61] S. Kotthaus, T. E. L. Smith, M. J. Wooster, and C. S. B. Grimmond, “Derivation of an urban materials spectral library through emittance and reflectance spectroscopy,” *ISPRS J. Photogramm. Remote Sens.*, vol. 94, pp. 194–212, Aug. 2014, doi: 10.1016/j.isprsjprs.2014.05.005.

Appendix A: Mathematical Energy-Balance Analysis

The energy balance for the black emitter and RC emitter is expressed in Equations (1) and (2) over a one-hour interval.

$$-mC_p(dT_{black}) = A \cdot \{P_{black} - P_{atm} - P_{ground} - P_{sun,black} - h\,(T_{amb} - T_{black})\} \cdot 3600 \quad \text{(A-1)}$$

$$-mC_p(dT_{RC}) = A \cdot \{P_{RC} - P_{atm} - P_{ground} - P_{sun,RC} - h\,(T_{amb} - T_{RC})\} \cdot 3600 \quad \text{(A-2)}$$

Subtracting Equation (A-2) from Equation (A-1) yields Equation (A-3).

$$-mC_p(dT_{black} - dT_{RC}) = A \cdot \{P_{black} - P_{RC} - P_{sun,black} + P_{sun,RC} - h\,(T_{RC} - T_{black})\} \cdot 3600 \quad \text{(A-3)}$$

At 12:00 under the trough-enhanced configuration, the global solar irradiance is 765 $W \cdot m^{-2}$, consisting of a direct component of 629.6 $W \cdot m^{-2}$ and a diffuse component of 135.4 $W \cdot m^{-2}$. The solar absorptance of RC emitter (α_{RC}) is 2 % while that of the black emitter (α_{black}) is 94 %. At a solar altitude of 60°, the two-dimensional geometric concentration factor (C_g) is 0.37. Accordingly, the absorbed solar power for each emitter is calculated as:

$$P_{sun,black} = \alpha_{black} \cdot (P_{direct} \cdot C_g + P_{diffuse}) = 346.3\ W \cdot m^{-2} \quad \text{(A-4)}$$

$$P_{sun,RC} = 7.4\ W \cdot m^{-2} \quad \text{(A-5)}$$

A wind speed of 0.8 $m \cdot s^{-1}$ corresponds to a convective heat-transfer coefficient of h = 20 $W \cdot m^{-2} \cdot K^{-1}$ based on the Churchill–Bernstein correlation. To simplify the analysis, it has been assumed that convection coefficient h is the same for both the RC and the black surface. The water specific heat capacity (C_p) is taken as 4.2 $kJ \cdot kg^{-1} \cdot K^{-1}$. Both emitters have surface area of A = 0.05 m^2, and the enclosed water mass is m = 0.6 kg. The measurements show that the water temperature increased by 1.8 °C for the RC emitter and by 4.8 °C for the black emitter between 11:00 and 12:00.

The radiative cooling powers P_{black} and P_{RC} were obtained using MCRT simulations at measured 12:00 temperature profile where T_{black} = 31 °C with P_{black} = 873.4 W·m^{-2}, and T_{RC} = 22 °C with P_{RC} = 771.5 W·m^{-2}

The equation (A-3) can be rewritten as follows:

$$-0.6 * 4200 * (4.8 - 0.8) = 0.05 * \left(873.4 - 771.5 - 346.3 + 7.4 - 20 * (22 - 31)\right) * 3600 \quad \text{(A-6)}$$

$$-7560\ \text{J} = -7020\ J \quad \text{(A-7)}$$

The resulting deviation is approximately 5%, demonstrating good consistency between the energy-balance prediction and the experimental measurements. The primary source of this deviation arises from the rough surface morphology of the porous RC membrane, which enhances convective heat transfer due to increased surface-induced turbulence. The remaining discrepancy can be attributed to uncertainties in temperature and wind-speed measurements, as well as minor errors in the optical property characterization of the materials.